

UNIVERSITA' DEGLI STUDI
DI PADOVA
Dipartimento di Fisica e Astronomia
Dipartimento di Ingegneria Industriale

ISTITUTO NAZIONALE
DI FISICA NUCLEARE

Laboratori Nazionali di Legnaro

MASTER THESIS/TESI DI MASTER

in

“Surface Treatments for Industrial Applications”

APPLICATION OF THE MAGNETRON SPUTTERING TECHNIQUE FOR THE DEPOSITION OF NIOBIUM ONTO COPPER RF CAVITIES FOR PARTICLE ACCELERATORS

Supervisor: Prof. V. Palmieri

Co-Supervisor: PhD. G. Keppel

Student: Andrii Tsymbaliuk

N. Matr.: 1160235

Academic Year 2016-2017

General content

List of tables	6
List of figures	7
INTRODUCTION	10
Chapter 1	12
Theoretical basis of superconductivity	12
1.1. Resonant cavities	12
1.2. Average accelerating field and quality factor	12
1.3. General properties of superconductors	12
1.4. Surface resistance	16
1.5. The residual surface resistance	17
1.6. Coherence length in superconductors	19
1.7. London Penetration depth.....	20
1.8. The skin effect in normal conducting case	21
Chapter 2	23
Theoretical basis of sputtering process.....	23
2.1. Mechanism and varieties of sputtering process	23
2.2. Advantages of sputtering process	24
2.3. DC magnetron sputtering	25
Chapter 3	27
High Vacuum Technologies	27
3.1. General information.....	27
3.2. Scheme of sputtering vacuum system	28
3.3. Creation of vacuum	29
3.3.1. Fore vacuum and high vacuum pumping	29
3.3.2. Mechanical pumps.....	31
3.3.3. Turbo Molecular Pumps	34

3.4. The measurement of low pressure	36
3.4.1. Overview	36
3.4.2. Indirect reading gauges (Pirani gauge).....	37
3.4.3. Bayard-Alpert hot cathode ionization gauge	38
3.4.4. Capacitance diaphragm gauge	39
3.5 Polycold gas chiller	39
Chapter 4	41
Niobium deposition onto 6 GHz cavities	41
4.1. Introduction	41
4.2. Methodology of Nb deposition onto the copper 6 GHz cavities	41
4.3. Using of magnetron in Nb sputtering system onto 6 GHz cavities	49
4.4. Experimental part	50
4.5. Conclusion to the chapter	58
Chapter 5	59
Nb deposition onto Quarter Wave Resonators (QWR)	59
5.1. Introduction	59
5.2. Methodology of preparation of the system for quarter wave resonator sputtering and holding of the Nb sputtering process	60
5.3. Using of magnetron in QWR sputtering system.....	66
5.4. Conclusion to the chapter	67
Chapter 6	68
Niobium deposition onto TESLA-type 9-cell RF cavities for particle accelerators	68
6.1. Introduction	68
6.2. Using of the quartz tube as the chamber of the vacuum system.	68
6.3. Outgassing curve of the system	70
6.4. First test with quartz shield.....	71
6.5. Second test with copper shield	75

6.6. Using of the magnetron in the system for niobium deposition onto TESLA-type 9-cell RF cavities	79
6.7. Test with final internal magnetron, assembled in the system.....	85
6.8. Deposition rate measurements.....	88
6.9. Conclusion to the chapter	88
CONCLUSION	91
Chapter 7	92
References	92

List of tables

Table 3.1 - Main characteristics of oil-sealed pumps	32
Table 3.2 - Various types of dry pumps	33
Table 4.1. - Parameters of the Nb coating deposition onto 6 GHz copper cavities	58
Table 5.2 – Parameters of the Nb deposition onto Quarter Wave Resonator.	66
Table 6.1 – Sputtering parameters during first test with quartz shield	74
Table 6.2 – Sputtering parameters during second test	78
Table 6.3 – Sputtering parameters during test of the new magnetron construction.....	87
Table 6.4 – Sputtering parameters during tests of deposition rate measurements	87

List of figures

Figure 1.1 - Meissner effect.	13
Figure 1.2 - Critical field versus temperature for some superconducting elements.....	14
Figure 1.3 - Magnetization versus magnetic field for superconductor type I.	15
Figure 1.4 - Critical magnetic field for superconductors type II.....	15
Figure 2.1. – Simplified cross section of the sputtering system.....	23
Figure 2.2 – Magnetron sputtering technique.	26
Figure 3.1 – Scheme of the sputtering system	28
Figure 3.2 – Pressure range, in which the use of various pumps is most economical	29
Figure 3.3 - The general qualitative relationship between pressure and flow for most compressors or pumps.....	30
Figure 3.4 – Rotor with different disk design	35
Figure 3.5 - Classification of Pressure Gauges	36
Figure 3.6 - Basic Pirani Gauge Circuit	37
Figure 3.7 - Bayard-Alpert Hot Cathode Ionization Gauge	38
Figure 3.8 - Nude Ionization Gauge.....	39
Figure 3.9 – Capacitance diaphragm gauge	40
Figure 4.1. – Connected Nb cathode to the cavity holder.	42
Figure 4.2. – Connected cavity to the cavity holder.....	42
Figure 4.3. – Sputtering system of Nb deposits onto 6 GHz copper cavities.....	43
Figure 4.4. – Baking zones of the sputtering system.	44
Figure 4.5. – Bottom part of the cavity stand.....	45
Figure 4.6. – Leak detection of the bottom part of the stand.	46
Figure 4.7. – Leak detection of the cavity stand.	47
Figure 4.8. – Assembling cavity stand into the cryostat.	48
Figure 4.9. – IR lamp in the chamber of additional baking.	49
Figure 4.10. – Cylindrical magnetron of the Nb sputtering system onto 6 GHz cavities.	50

Figure 4.11. – Dependence of the quality factor from the energy of accelerating field, that was obtained during measurements in cryostat at 4.2 K and 1.8 K.	51
Figure 4.12. – Temperature and pressure dependence from the time during holding cryostat measurements of the experiment # 1.....	51
Figure 4.13. – Radiation dependence from the time during holding cryostat measurements of the experiment # 1.....	52
Figure 4.14. – Dependence of the quality factor from the energy of accelerating field, that was obtained during measurements in cryostat at 4.2 K and 1.8 K at the experiment #2 after all after sputtering operations.	53
Figure 4.15. – Dependence of the quality factor from the energy of accelerating field, that was obtained during measurements in cryostat at 4.2 K and 1.8 K at the experiment #3.....	54
Figure 4.16. – Dependence of the quality factor from the energy of accelerating field, that was obtained during second measurements in cryostat at 4.2 K at the experiment #3	54
Figure 4.17. – Dependence of the quality factor from the energy of accelerating field, that was obtained during third measurements in cryostat at 1.8 K and 4.2 K at the experiment #3.	55
Figure 4.18. – Dependence of the quality factor from the energy of accelerating field, that was obtained during measurements in cryostat at 4.2 K at the experiment #4.	56
Figure 4.19. – Dependence of the quality factor from the energy of accelerating field, that was obtained during measurements in cryostat at 4.2 K at the experiment #5.	56
Figure 4.20. – Dependence of the quality factor from the energy of accelerating field, that was obtained during measurements in cryostat at 4.2 K at the experiment #6.	57
Figure 5.1 – Low and high β cavities [3]	60
Figure 5.2 – System for QWR sputtering.....	61
Figure 5.3 – Test heating of the system	62
Figure 5.4 – Water cooling system of the magnetron	63
Figure 5.5 – Argon plasma, that was observed during the sputtering process.....	64
Figure 5.6 – Baking of the system	65
Figure 6.1 – Crack of the quartz tube.....	69
Figure 6.2 – New aluminium flange design	70
Figure 6.3 – Outgassing curve, obtained without baking.....	71

Figure 6.4 - 6 GHz cathode Niobium cavity assembly with quartz shielding	72
Figure 6.5 - Plasma during first sputtering test using 6 GHz cavity as cathode.	73
Figure 6.6 - Sputtered quartz tube after holding of the first test	74
Figure 6.7 - Particular of copper tube with holes for holding quartz samples	75
Figure 6.8 - Quartz samples fixed onto the Cu tube.....	76
Figure 6.9 - Section of 6 GHz test magnetron simulating the copper cavity.	77
Figure 6.10 - Left: picture of the copper shield assemblies on the system, on the centre 6 quartz samples are visible. Right: a detail of the upper centring system of the Cu tube.	77
Figure 6.11 - Argon plasma inside the copper tube during sputtering process.....	78
Figure 6.12 - Magnetron optimized for coating 9-cell cavity. The cathode is composed by nine 6 GHz cavities connected by Nb Tube. Eight SS rods support the copper cavity. On the bottom is visible the cavity centring system.	79
Figure 6.13 - Detail of the magnetron. The spiral of external inductors is visible. Inside the quartz tube is visible the 9-cell copper cavity and the 6 GHz niobium cathode	80
Figure 6.14 - Rendering of the top magnetron flange. From the top is visible the rotating feedthrough that permits rotation of the magnets and at the same time water insulation, after the special aluminium components designed in order to water cool the magnetron.	82
Figure 6.15 - Rotating magnetron for 9-cell cavity. In the centre of the cavity is visible the Nb cathode with inside the water-cooled rotating magnet.....	83
Figure 6.16 - Rendering of Nylon magnets holder rotated. In red the north pole of magnet, in blue south pole.	84
Figure 6.17 - Nylon 6 magnet pack assembled. On left front view, on right rear view.....	85
Figure 6.18 - Cathode assembled and ready for insertion inside the quartz vacuum chamber..	86
Figure 6.19 - Two different views of the plasma inside the vacuum chamber during preliminary test.	87
Figure 6.20 – Deposition rate of the system, that was measured at different sputtering parameters	89

INTRODUCTION

In the end of 1950-s scientific society faced with the problem of kinematic inefficiency of great proton accelerators, that dominated in particle and nuclear physics. These machines accelerated protons up to their maximum energy (26 GeV for the CERN PS) after which they were extracted from the machine and brought into collision with the nuclei of particles in a “fixed target”. Most of the beam energy is used in moving the target nucleon forward. Only a fraction is available for making new particles. So, in order to improve technology of great proton accelerators emerged the idea of colliding two beams travelling in opposite directions. With this modification available energy increased. It was first step on the road of building the Large Hadron Collider.

The LHC was built between 1998 and 2008. The main purpose of the biggest collider in the world is to find answers on some of the fundamental opened questions in physics, concern the basic laws governing the interactions and forces among the elementary objects, the deep structure of space and time, and in particular the interrelation between quantum mechanics and general relativity [1].

The International Linear Collider is the new step of understanding the world in nuclear physics. Consisting of two linear accelerators that face each other, the ILC will hurl 10 billion electrons and their anti-particles, positrons, toward each other at nearly the speed of light. Stretching approximately 31 kilometres in length, the beams collide 14,000 times every second at extremely high energies – 500 billion-electron-volts (GeV). The current baseline design allows for an upgrade to a 50-kilometres, 1 trillion-electron-volt (TeV) machine during the second stage of the project. There are also plans for a staged approach starting with a 250-GeV Higgs factory to study the properties of the particle discovered at the LHC in 2012 and then upgrading to 500 GeV in order to make deeper study of the discovered particles [2].

Niobium cavities will be used for super conductive particle accelerators. One of the main challenges is replacing Nb bulk cavities onto Cu cavities, sputtered by the thick Nb layer. In order to improve technology of vacuum sputtering Nb onto copper cavities the researching work was held.

Many research institutions have studied the sputtering technology applied to complex substrates. The development of the deposition of Niobium onto copper cavities started at CERN from 1980, as a method to replace bulk cavities. Then, at Legnaro National Laboratories (LNL), since 1987 it has been studied the bias diode sputtering in order to deposit Niobium onto copper QWRs for the construction of ALPI accelerator, obtaining positives results: good film uniformity and good performance but lower deposition rates in comparison with other techniques such as magnetron sputtering technique [3].

The magnetron sputtering is a deposition technique widely used in the thin film industry because of advantages of this method.

In the Legnaro National Laboratories were developed three different types of cavities: TESLA-type 9-cell RF cavities, Quarter Wave Resonators, 6 GHz cavities. For each type different magnetron sputtering technique is applied. The aim of the investigation is to analyse the influence of the different magnetron configurations on the Nb sputtering for every type of the developed cavities.

Chapter 1

Theoretical basis of superconductivity

1.1. Resonant cavities

A key component of the modern particle accelerator is the device, that imparts energy to the charged particles. This is an electromagnetic cavity resonating at a microwave frequency. A resonant cavity is an energy storage device employed for the radiofrequency and microwave range. It is equivalent to a classical RLC resonant circuit.

At low frequencies the parallel-connected capacitor and will resonate at a frequency $\omega_0 = 1/\sqrt{LC}$. To make this circuit resonating at higher frequencies, a possibility is to decrease L as much as possible [4].

1.2. Average accelerating field and quality factor

The two most salient characteristics of accelerating cavity are its average accelerating field, E_{acc} , and the quality factor Q_0 , which is the intrinsic Q of the resonant cavity. The quality factor is a universal figure of merit for resonators and is defined in the usual manner as the ratio of the energy stored in the cavity (U) to the energy lost (P_c) in one rf period. It measures the number of oscillations a resonator will go through before dissipating its stored energy. The Q_0 depends on the microwave surface resistance of the metal. In general, one would like to have an accelerating field and a Q_0 as high as possible. The intrinsic bandwidth of a resonator is inversely proportional to Q_0 . Values of Q_0 as high as 10^{11} have been reached [5].

1.3. General properties of superconductors

In 1911 H. Kamerling Onnes, studied the electrical resistance of mercury with the temperature observing that the resistance dropped sharply to zero at a temperature of 4,2K. The same properties were later discovered in some other metals. The phenomenon was named “superconductivity” and the corresponding metals were called “superconductors”.

The temperature at which the resistance is close to zero is called critical temperature T_c and it is different in each material with superconductive properties. The highest critical temperature between pure metals is shown by niobium, $T_c=9,25K$; and the lowest has been found by β -phase of tungsten, $T_c=0,0154K$. However, these are both low temperatures and the temperature range is very wide, since the two extremes differ by about a factor of a thousand.

K. Onnes in 1914, has carried out subsequent investigations about superconductive properties. He has shown that superconductivity can be destroyed not only by increasing the temperature and

also by applying a sufficiently strong magnetic field. The critical field (H_c) in which the superconductivity is destroyed decreases with the increment of temperature. The following formula describes empirically the dependence $H_c(T)$.

$$H_c(T) = H_c(0) \left[1 - \left(\frac{T}{T_c} \right)^2 \right] \quad (1.1)$$

Also the superconductivity can be destroyed by a strong electric current. If the superconductor is not too thin, the magnetic field produced by a critical current must be equal to zero at the surface of a superconductor.

Meissner and Ochsenfeld in 1933, have discovered another superconductive property. If a metal is placed in a magnetic field smaller than H_c , then during the transition into the superconducting state the field is expelled from its interior; the true field or magnetic induction B that is the average microscopic field is zero in the superconductor. This effect is called Meissner effect. (See Figure 1.1).

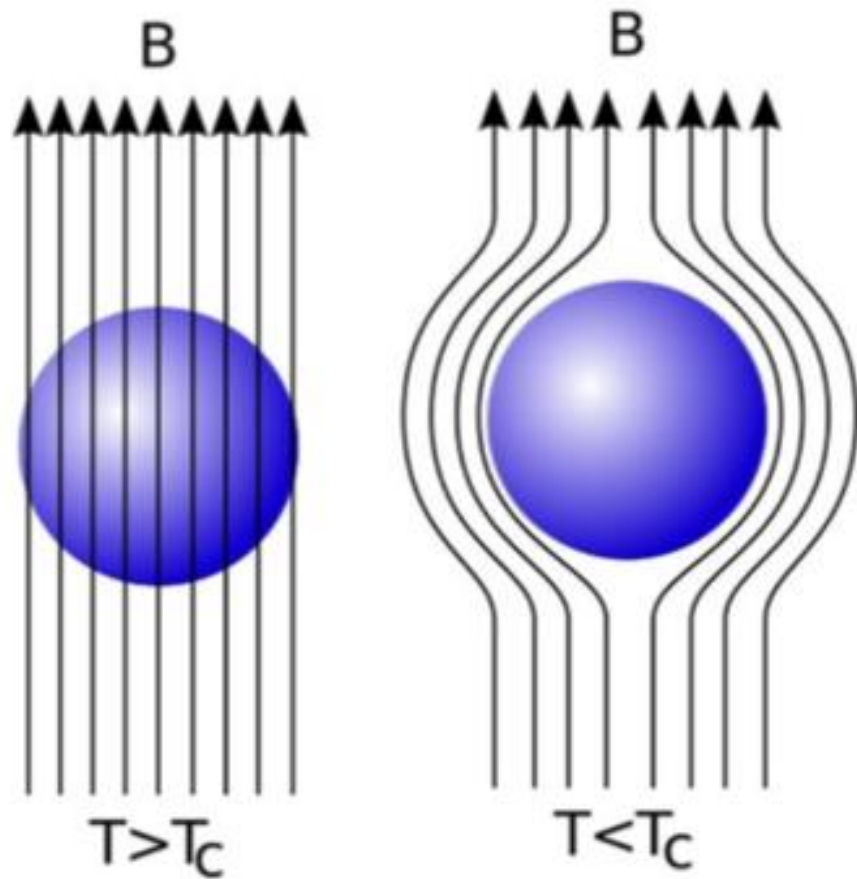


Figure 1.1 - Meissner effect.

In more detailed investigations it has been shown that only in the bulk of a massive sample the magnetic field is equal to zero. In a thin layer which is called penetration depth (λ), the field decreases gradually from a given value to zero. The thickness of this layer is usually of the order of $1 \cdot 10^{-5}$ to

$1 \cdot 10^{-6}$ cm. If a superconductor is placed in an external magnetic field, currents appear in the surface layer, producing a magnetic field on its own, that compensates the external field inside the superconductor

There are two types of superconductors. The first one is the superconductor type I, mainly comprised of metal sans metalloids that have two characteristic properties: Zero DC electrical resistance and perfect diamagnetism when the material is cooled below a critical temperature T_c . Above T_c the material is not a very good conductor but is a normal metal. The second property is the perfect diamagnetism or also called Meissner effect, explained before.

The behaviour of a superconductor type I is approximated by a parabola, and defines the limit of presence of superconductivity. It can be a sharp transition from the superconducting state to the normal one, as can be seen in Figure 1.2.

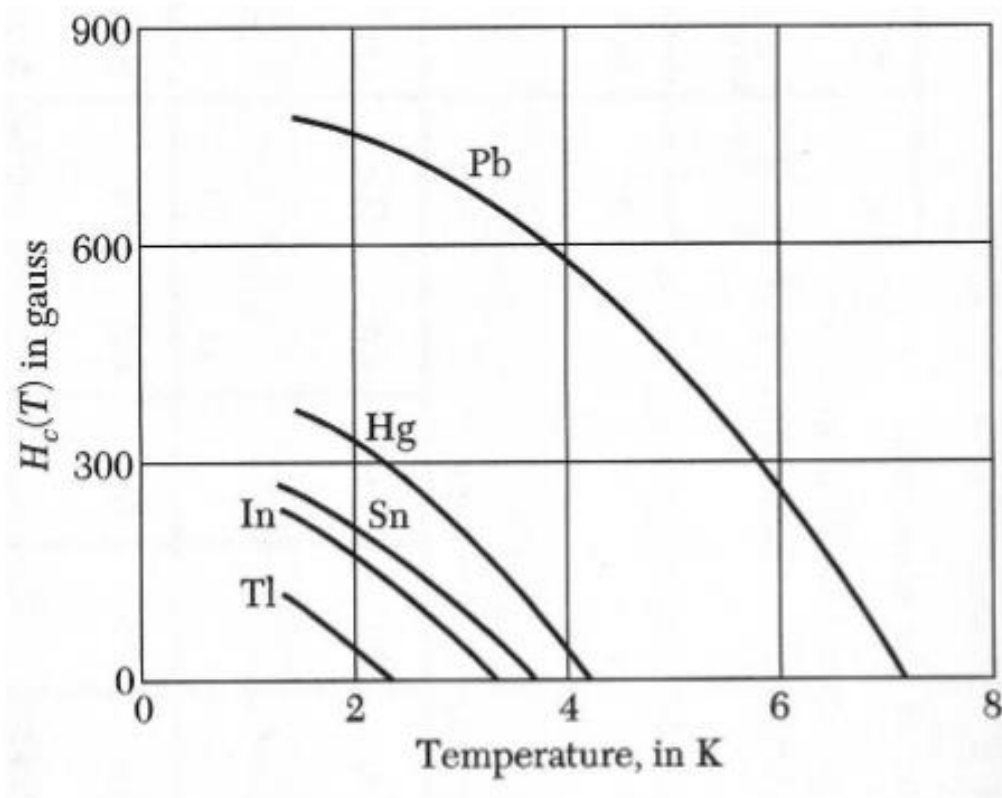


Figure 1.2 - Critical field versus temperature for some superconducting elements.

The same transition can be seen drawing the magnetization versus the magnetic field.

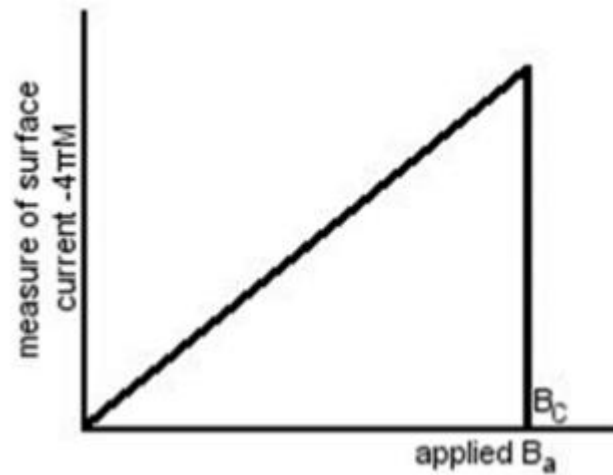


Figure 1.3 - Magnetization versus magnetic field for superconductor type I.

The magnetization in the superconducting state is equal to $-H/4\pi$, while is zero in the normal state. The critical field of this type of superconductor is quite low (approximately less than 10^{-1} Tesla).

Superconductors type II are usually alloys and compounds. They have a high critical fields and high critical currents. The characteristic of this kind of superconductor is the magnetic behaviour. They have two critical fields H_{c1} (T), below which the material is totally superconducting and H_{c2} , that is the upper critical field over which the material is entirely normal conducting. (See Figure 1.4).

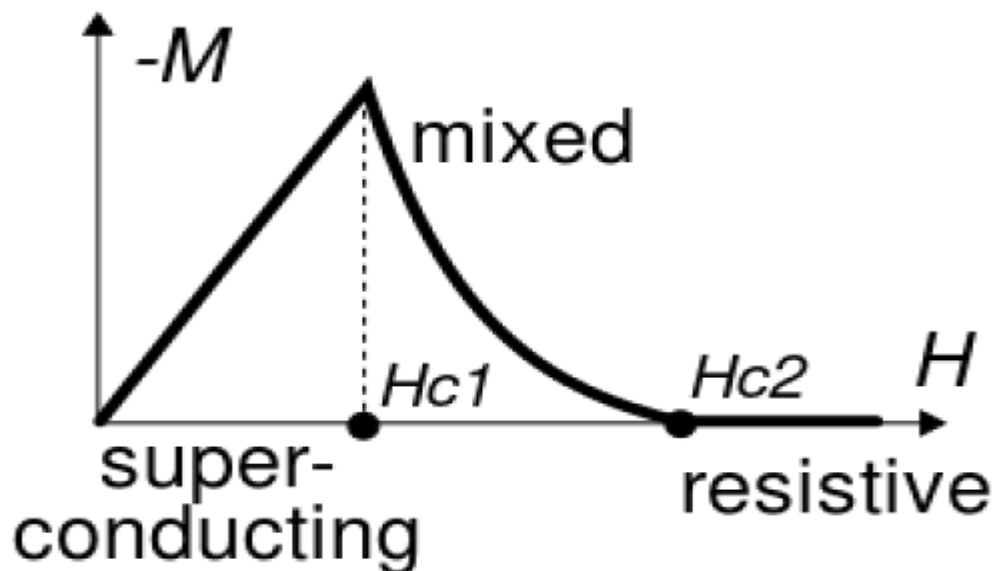


Figure 1.4 - Critical magnetic field for superconductors type II.

In previous figure it can be seen the magnetization versus field for a second type superconductor, where shows an incomplete region of Meissner-Ochsenfeld effect.

Superconductors of second type are also perfect conductors of electricity (with zero DC resistance). It totally excludes the magnetic field in the Meissner state when the applied magnetic field is below the lower critical field, then when the applied field is between H_{c1} and H_{c2} the flux is partially excluded and above this field the material becomes normal conductor. The sample shows an incomplete Meissner state in which there is a partial penetration of magnetic flux in a complicated microscopic structure of thin normal conducting filaments surrounded by superconductive regions. Such kinds of filaments are called “vortexes”.

Fundamentally, a superconductor can be defined as a conductor that has a phase transition below a transition temperature T_c in which the conduction electrons form pairs called “Cooper pairs”, which can carry electrical current without any resistance to the flow and which are also responsible for the perfect diamagnetism [3].

1.4. Surface resistance

The remarkable properties of superconductivity are attributed to the condensation of charge carries into Cooper pairs. At $T = 0$ K, all charge carries are condensed. At higher temperatures, some carries are unpaired; the fraction of unpaired carries increases exponentially with temperature until none of the carries are paired above T_c . The pairs move frictionlessly. In this simplified picture, known as the London two-fluid model, when a dc field is turned on, the pairs carry all the current, shielding the applied field from the normal electrons. Electrical resistance vanishes.

In the case of rf currents, however, dissipation does occur for all $T > 0$ K, though very small compared to the normal conducting state. A simple expression for the rf surface resistance is

$$R_s = A \left(\frac{1}{T} \right) f^2 \exp \left(- \frac{\Delta(T)}{kT} \right) + R_0 \quad (1.2)$$

Here A is a constant, dependent on the material parameters of the superconductor, such as the penetration depth, $\lambda_L(0)$, the coherence length, ξ_0 , the Fermi velocity, v_F , and the mean free path, l . 2Δ is the energy gap of the superconductor, i.e., the energy needed to break the pairing. Equation (1.2) fits the experimental results for frequency and temperature dependence remarkably well for $T < 0.5T_c$. The quadratic frequency dependence and the exponential temperature dependence of the first term of equation (1.2) are easy to see with the two-fluid model. While the Cooper pairs move frictionlessly, they do have inertial mass. This means that for high-frequency currents to flow, forces must be applied to bring about alternating directions of flow. Hence ac electric field will be present

in the skin layer and they will continually accelerate and decelerate the normal carriers in the skin layer, leading to dissipation. The power dissipated is proportional to the internal electric field and to the normal component of the current. The interior electric field, induced by the changing magnetic field, is proportional to the rf frequency, f . The “normal” component of the current also depends on the number of carriers thermally excited across the energy gap, 2Δ , and is given by the Boltzmann factor $\exp(-\Delta/kT)$ [5].

The operating temperature of a superconducting cavity is usually chosen so that the first term in equation (1.2) is reduced to an economically tolerable value. R_0 , referred to as residual surface resistance, is discussed in the next chapter.

1.5. The residual surface resistance

The term “residual” is an indication that the causes of those losses are often not clear. Indeed, even if much is reported in literature about the possible origins of the non-BCS losses, they are far from being completely understood, mainly because both “physical phenomena” and “accidental mechanisms” contribute to the residual. In particular, the “accidental mechanism” makes difficult to identify the physical cases from the experimental results that often are not highly reproducible even for the same cavity when it cooled and measured several times.

There is the list of the possible sources of residual losses which were more investigated and discussed among the others:

- a) Losses due to a non-ideal surface quality:

The non-controllable nature of this kind of losses makes them rather difficult to analyse. On the other hand, it is universally recognised that the worst polished superconducting surface shows the higher residual losses. The enhanced phonon generation taking place on real surface due to the unavoidable presence of surface irregularities is proposed in literature as a possible physical mechanism responsible for such type of dissipations.

Inclusion of metallic foreigner particles into the superconductor within a London penetration depth λ from the surface can also be source of Joule losses. Depending on the thermal conductivity of the superconductor and on the contact thermal resistance between the normal particles and the superconductor, normal area will dissipate more and more, as soon as power is injected into the cavity. If the thermal conductivity of the surrounding material is not high enough to remove the heat developed by normal islands to the liquid helium bath, the local temperature gets higher and higher. As a result the critical field gets lower and lower. All this can result into a sudden transition from the normal state to the superconducting state (quench) and can constitute a severe limitation to the achievement of high field inside superconducting resonators.

b) Losses due to an Oxide layer present on the superconducting surface:

It must be kept in account that the only two superconductors most widely used for superconducting cavities applications are Lead and Niobium. Without doubt when high performance resonators are required, the Niobium choice becomes compulsory. Respect to Lead indeed Niobium has a 2K higher critical temperature, and a critical field H_c at 0K of 2000 Gauss against only 800 Gauss of Lead. Moreover, Niobium is superior to Lead even from the surface stability point of view: Lead has several stable oxides; Niobium has only two oxides Nb_2O_5 and NbO . Due to the too small thickness of saturation, NbO plays a minor role in the mechanism of rf losses. Nb_2O_5 also is recognised to be not significant from the point of view of rf residual losses, since for example, as indicated by Halbritter only fractions of $n\Omega$ are expected in a 6 nm defect free Nb_2O_5 layer.

On the contrary a possible source for residual losses can be represented by the interface suboxide precipitates mainly between Nb grains and NbO . An Oxygen content of only 1 at. % dissolved inside Niobium indeed reduces the critical temperature T_c by 10%.

c) Losses due to electromagnetic generation of acoustic phonons:

If the action of transverse radiofrequency fields on the lattice ions are considered, the generation of transverse ultrasonic oscillations becomes important and the conversion efficiency of electromagnetic to acoustic energy rapidly increases in the GHz range at low temperatures when increasing the purity of the material.

d) Losses due to the trapping of magnetic flux:

Trapped flux losses due only to the background earth field have been universally recognized as a primary source of residual losses. Because of the large demagnetization factor of the extended surface of a resonator, an incomplete Meissner-Ochsenfeld effect happens, favouring the trapping into the superconductor of any external field present during the cooling phase. The adoption of Helmholtz coils or high magnetic permeability screens around cryostat in fact sensitively improves the rf performance of superconducting cavities.

e) Losses due to the superconductor polycrystallinity:

For type II superconductors the rf and microwave surface impedance can be strongly limited by dissipative process determined by the intergranular coupling. Additional surface resistance can indeed arise due to the nature of grain boundaries behaving as weak links of Josephson junctions. Such mechanism has been firstly considered for high T_c superconductors, recently it has been investigated for Niobium.

f) Losses due to the Hydrogen segregation:

A nouvelle kind of additional losses during last few years has been recently recognised to be, in particular for Niobium cavities, a potential enemy to fight. It is well-known that Niobium, if

electropolished or chemically treated by immersion in Hydrogen-rich etchant can be charged at least on surface by Hydrogen.

Hydrogen mobility in Niobium is known to be very high; moreover, it is clear that if diffusion there is, it will happen through grain boundaries rather than through single grains. Hydrogen should first enter into Niobium interstitially at room temperature and then precipitate to form Hydride island randomly distributed inside Niobium, when cooled below 120 K.

This hypothesis might explain the so-called “Q-disease” and the “100 K effect” for Niobium cavities, i. e. the deterioration of Q versus field depending on the particular chemical treatment or on the cooling rate especially observed after a long warm-up of the cavity at about 100 K. The hypothesis of the hydrogen effect on the cavities performances is certainly interesting. However, much work still must be done for arriving to a full confirmation and understanding of the real effects of Hydrogen.

g) General considerations about the residual losses:

It is not possible to give one formula predicting the residual losses, since their potential sources are too many and often too fragmentary information exist about them [4].

1.6. Coherence length in superconductors

A very successful microscopic theory was developed by Bardeen, Cooper and Schrieffer which is called BCS- theory for classical superconductors like lead or tin. They assumed that electrons begin to condense below T_c to pairs of electrons, the called Cooper pairs. The two electrons in a pair have opposite momentum and spin. They experience an attractive force mediated via quantized lattice vibrations called phonons. This bound state of the two electrons is energetically favorable. As the overall spin of these two paired electrons is zero, many of these pairs can co-exist coherently, just like other bosons. The coherence length describes the distance over which the electrons are correlated. It is given by:

$$\xi_0 = \frac{\hbar v_f}{\Delta} \quad (1.3)$$

Where (v_f) is the Fermi velocity that represents the velocity of the electrons close to the Fermi energy and $2 \cdot \Delta$ is the energy necessary to break up a Cooper pair. Typical values for the coherence length in niobium are around 39 nm.

1.7. London Penetration depth

Respect type I superconductor, the magnetic field is not completely expelled, but penetrates inside the material over a small distance, otherwise the shielding current density would be infinitely large. The distance called “London penetration depth” is given by the characteristic length of the exponential decay of the magnetic field inside the superconductor.

$$H(x) = H(0)e^{\frac{-x}{\lambda_l}} \quad (1.4)$$

The penetration depth value is:

$$\lambda_l = \sqrt{\frac{m}{\mu_0 n_s e^2}} \quad (1.5)$$

Where e is the charge of an electron, m is the mass and n_s the number of superconducting charge carriers per unit volume. A typical value for the penetration depth in niobium is 32 nm.

The theory did not allow for impurities in the material nor for a temperature dependence of the penetration depth. The scientists Gorter and Casimir introduced the two-fluid model where a coexistence of a normal- and superconducting fluid of charge carriers is postulated.

$$n_c = n_s + n_n \quad (1.6)$$

They suggested a temperature dependence of the superconducting charge carriers.

$$n_s(T) = n_s(0) \left(1 - \left(\frac{T}{T_c}\right)^4\right)^{-\frac{1}{2}} \quad (1.7)$$

Combining the last two equations, the penetration depth shows the following temperature dependence:

$$\lambda_l(T) = \lambda_0 \left(1 - \left(\frac{T}{T_c}\right)^4\right)^{-\frac{1}{2}} \quad (1.8)$$

The Ginzburg-Landau parameter is defined as:

$$k = \frac{\lambda_l}{\xi_0} \quad (1.9)$$

κ is a parameter that allows to identify the two types of superconductors:

$$k < \frac{1}{\sqrt{2}} \quad \text{superconductor type I} \quad (1.10)$$

$$k > \frac{1}{\sqrt{2}} \quad \text{superconductor type II} \quad (1.11)$$

Niobium has $\kappa \approx 1$ and is a weak type-II superconductor. The role of impurities was studied by Pippard; the study was based on the evidence that the penetration depth depends on the mean free path of the electrons in the material. The dependence of ξ on the mean free path is the following.

$$\frac{1}{\xi} = \frac{1}{\xi_0} + \frac{1}{l} \quad (1.12)$$

He introduced an effective penetration depth:

$$\lambda_{eff} = \lambda_l \cdot \left(\frac{\xi_0}{\xi}\right)^{\frac{1}{2}} \quad (1.13)$$

Here again ξ_0 is the characteristic coherence length of the superconductor. This relation reflects that the superconducting penetration depth increases with a reduction of the mean free path. For pure (“clean”) superconductor ($\ell \rightarrow \infty$) one has $\xi = \xi_0$. In the limit of very impure (“dirty”) superconductors where $\ell \ll \xi_0$, the relation becomes instead

$$\xi = \ell \quad (1.14)$$

The mean free path in the niobium is strongly influenced by interstitial impurities like oxygen, nitrogen and carbon.

As was proved after, (1.7) equation do not exactly describes experimentally obtained dependence. Real mathematic description of the dependence is the following:

$$n_s(T) = n_s(0)e^{-\frac{\Delta(T)}{kT}} \quad (1.15)$$

1.8. The skin effect in normal conducting case

If a RF electromagnetic field is oscillating inside the cavity, only the electrons of a thin layer called skin depth on the resonator walls, are interacting with the radiofrequency field and the loss are confined in such a layer.

There is an analogy between the shielding mechanism of a microwave field in a normal conductor and the shielding of a static magnetic field in a superconductor. If a microwave of frequency is incident on a metal surface, the field decays over a distance (skin depth). If the frequency is much lower than plasma frequency, the mean free path of the electrons is smaller than the penetration depth. Penetration depth can be calculated in the next way:

$$\delta = \sqrt{\frac{2}{\sigma \mu_0 \omega}} \quad (1.16)$$

Where σ is the conductivity of the metal. In this regime, the skin effect is shown. The surface resistance can be calculated by the formulae:

$$R_{surf} = \frac{1}{\sigma \delta} \quad (1.17)$$

In this case the resistance decrease at cryogenic temperatures because σ increase when $T \rightarrow 0$. Respect pure metals, at low temperatures ℓ may be larger than δ which leads to the anomalous skin effect; in this case the electrons can be scattered not only by phonons but by impurities in the lattice [3]. The resistance when $\ell \rightarrow \infty$ is represented for the following equation:

$$R_{surf} = \left[\sqrt{3\pi} \left(\frac{\mu_0}{4\pi} \right)^2 \right]^{\frac{1}{3}} \omega^{\frac{2}{3}} \left(\frac{\ell}{\sigma} \right)^{\frac{1}{3}} \quad (1.18)$$

That means, that even at the low temperature it will be always big R_{surf} because of the increasing of σ . That's why, for obtaining RF cavities with quality factor $Q \sim 10^9$ super conductivity is mandatory.

Chapter 2

Theoretical basis of sputtering process

2.1. Mechanism and varieties of sputtering process

If a solid or liquid at any temperature is subjected to bombardment by suitable high energy atomic particles (usually ions), it is possible for individual atoms to acquire enough energy via collision processes to escape from the surface. This means of causing ejections of atoms from a surface is called sputtering. Just as atoms ejected from the surface by evaporation can be used in deposition a coating on a substrate. Any suitable energetic atomic particles impinging against a surface can cause sputtering. It is most convenient to accelerate ions to energies suitable for sputtering so we henceforth speak only of sputtering under ions bombardment [6].

Figure 2.1 represents a greatly simplified cross section of a sputtering system. Typically, the target (a plate of the material to be deposit or the material from which a film is to be synthesized) is connected to a negative voltage supply (dc or rf). The substrate holder faces the target: the holder can be grounded, floating, biased, heated, cooled, or some combination of these. A gas is introduced to provide a medium in which a glow discharge can be initiated and maintained. Gas pressures ranging $1 \div 100$ mbar are used. The most common sputtering gas is Argon.

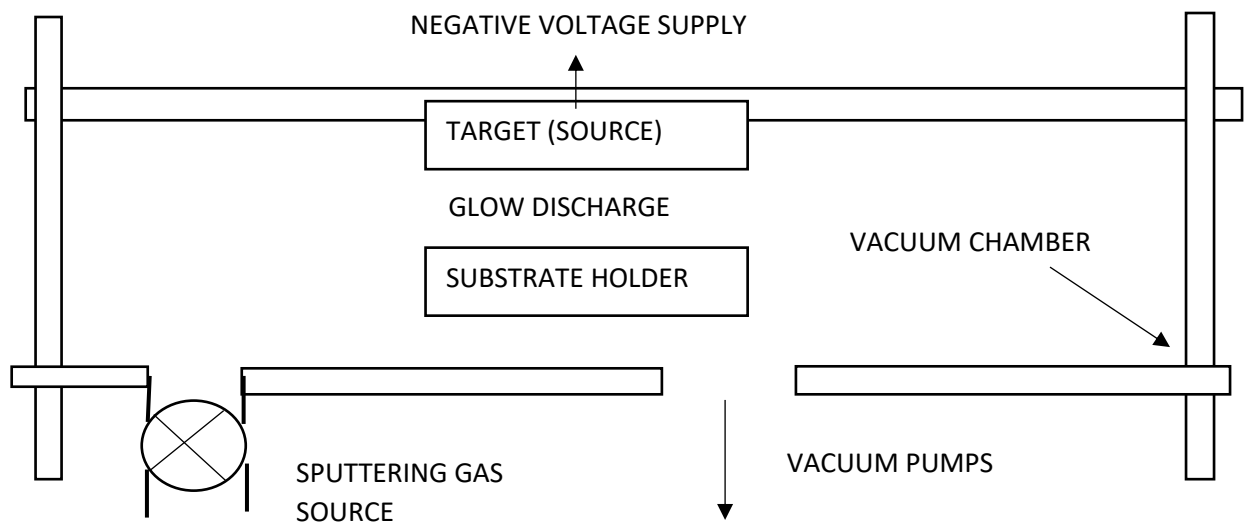


Figure 2.1. – Simplified cross section of the sputtering system.

When the glow discharge is started, positive ions strike the target plate and remove mainly neutral target atoms by momentum transfer, and these condense into thin films. There is, in addition, other particles and radiation produced at the target, all of which may affect film properties (secondary

electrons and ions, desorbed gases, x rays and photons). The electrons and negative ions are accelerated toward the substrate platform and bombard it and the growing film. In some instances, a bias potential (usually negative) is applied to the substrate holder, so that the growing film is subject to positive ion bombardment. This is known variously as bias sputtering or ion plating. Initially, the term “ion plating” referred to a process in which the deposition source was a thermal evaporation filament instead of a sputtering target and the substrates were connected to a dc sputtering target, but it has sometimes been applied to any process in which the substrate is subjected to purposeful ion bombardment during film growth in a glow discharge environment.

In some cases, gases or gas mixtures other than Ar are used. Usually this involves some sort of reactive sputtering process in which a compound is synthesized by sputtering a metal target (i.e., Ti) in a reactive gas (e.g., O₂ or Ar – O₂ mixtures) to form a compound of the metal and the reactive gas species (e.g., TiO₂). Reactive sputtering is also used to replenish constituents of compounds targets lost by dissociation. The reactive version of ion plating is sometimes known as activated reactive evaporation, but this terminology is more often applied to processes in which an evaporant passes through a glow discharge in transit to an electrically floating or grounded substrate. Reactive sputtering should not be confused with chemical sputtering in which the reactive gas (e.g., O₂) reacts with the target surface (e.g., C) to form volatile compounds (e.g., CO) that are pumped away. Chemical sputtering is more properly related to ion etching processes [6].

2.2. Advantages of sputtering process

Unique characteristics of sputtering

1. Deposition rates is different in different materials, but it can be calculated and managed. This is often a useful feature in multilayer deposition.
2. Deposition rates by sputtering are much lower for some materials and much higher for other materials than deposition rates by evaporation.
3. Thickness control is very simple. After a calibration run has been made, thickness control is merely a matter of setting a timer.
4. The lifetime of a sputtering target may be as long as hundreds of run and is seldom less than 20. This is in sharp contrast to evaporation, where a source of seldom lasts as long as 10 runs.
5. In sputtering alloys and other complicated materials, the deposition maintains stoichiometry with the original target composition. No other method can be used to deposit alloys.

6. Cleaning of parts and substrates by reverse sputtering is an advantage that can be gained with no other process. One can combine sputter-cleaning with vacuum evaporation, but this obviously tends to complicate operations.

7. The problem of spitting (ejection of particles from sources during evaporation) does not occur in sputtering.

8. The high ejection energy of sputtered atoms (~ 10 eV) is often suggested as a factor in improving film structure and adhesion to the substrate. This is not very likely to be a detectable factor. It is our experience, that where sputter-cleaning is not used, the adhesion of a given material to a given substrate is the same for sputtered deposits as for evaporated deposits [6].

2.3. DC magnetron sputtering

In order to get high sputtering rates and good film performance, DC magnetron sputtering is widely used.

As was explained before, in the mechanism and varieties of the sputtering process, a target (called cathode) plate is bombarded by energetic ions generates in a glow discharge plasma, situated close to the target. The bombardment process causes the removal or sputtering of target atoms that can condense on a substrate as a thin film.

Secondary electrons can be emitted from the target surface due to the ion bombardment and these electrons play an important role to maintain the plasma. The sputtering process has been used for many years and many applications however this process is limited by low deposition rates, low ionization efficiencies in the plasma and high substrate heating effects. This limitation has been overcome by the development of magnetron sputtering.

The magnetron target is based on the work carried out by Penning more than 60 years ago, however the planar magnetron, which is the most widely used target assembly was not introduced until 1970.

Magnetron sputtering involves placing magnets behind the sputtering target. The resulting magnetic field influences the trajectories of moving charge particles by the Lorentz force. The result is the confinement of the electrons near to the sputtering target that increases the ionization in the working gas.

Magnetrons uses the fact that a magnetic field configured parallel to the target surface can constrain secondary electron motion to the vicinity of the target. In the planar magnetron the magnets are arranged positioning one pole at the central axis of the target and the second pole is formed by a ring of magnets around the outer edge of the target. Trapping the electrons in this way it is possible to increase the probability of ionization that results in a dense plasma in the target region. This in

turn, leads to increased ion bombardment of the target, giving higher sputtering rates and also higher deposition rates at the substrate. In addition, the efficiency of this process allows the discharge to be maintained at lower operation pressures (typically, 10^{-3} mbar, compared to 10^{-2} mbar) and lower operating voltages (typically, -500V, compared to -2 to -3 kV of the diode) than basic sputtering mode.

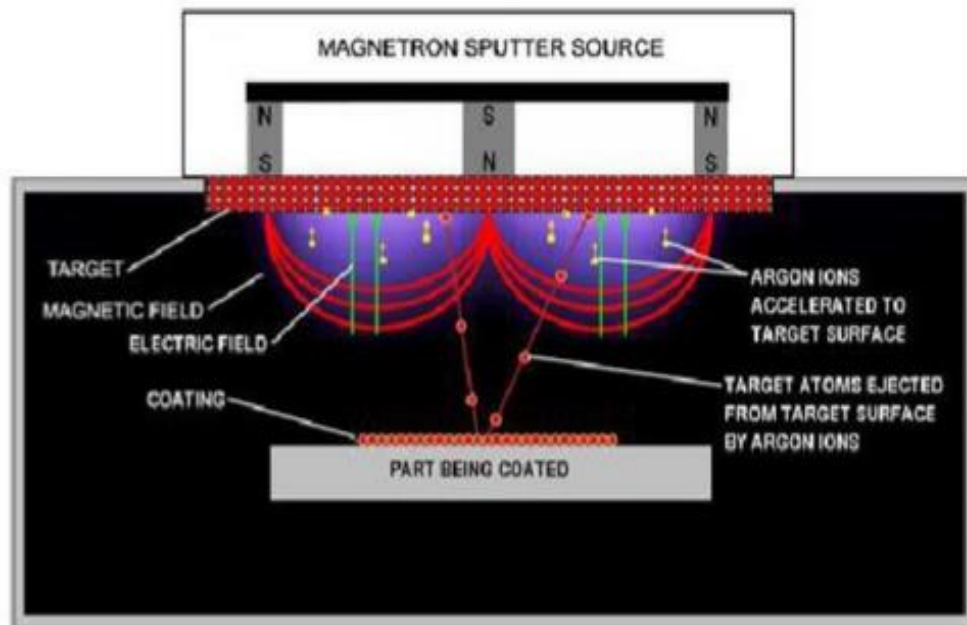


Figure 2.2 – Magnetron sputtering technique.

The efficiency of the available electrons can be incremented by a magnetic field parallel to the cathode surface that confines the plasma. A general rule for the shape of the magnetic field is:

- 1) “The magnetic field must born from the cathode and die onto the target”.
- 2) A plasma confinement is achieved, while magnetic and/or electrostatic mirrors trap the electrons. The magnetic field traps and forces the electrons to describe helical paths around the lines of magnetic path. When vectors B and E the particles are freely accelerated, while when there is an electric field component E_{\perp} (Volts/cm) perpendicular to B , a drift of speed VE occurs [3].

Chapter 3

High Vacuum Technologies

3.1. General information

The term vacuum is generally used to denote a volume or region of space in which the pressure is significantly less than 1000 mbar. In the traditional measurement system, normal pressure is expressed in millimeters of a column of mercury, and 760 millimeters of mercury is equal to 1 standard atmosphere. A perfect or absolute vacuum, which implies a space that is entirely devoid of matter, is practically unrealizable. For practical purposes, however, and in accordance with the definition proposed by the American Vacuum Society, the term vacuum is generally used to denote a space filled with a gas at less than atmospheric pressure. In the metric, or meter-kilogram-second (MKS), system, the unit of pressure is the pascal.

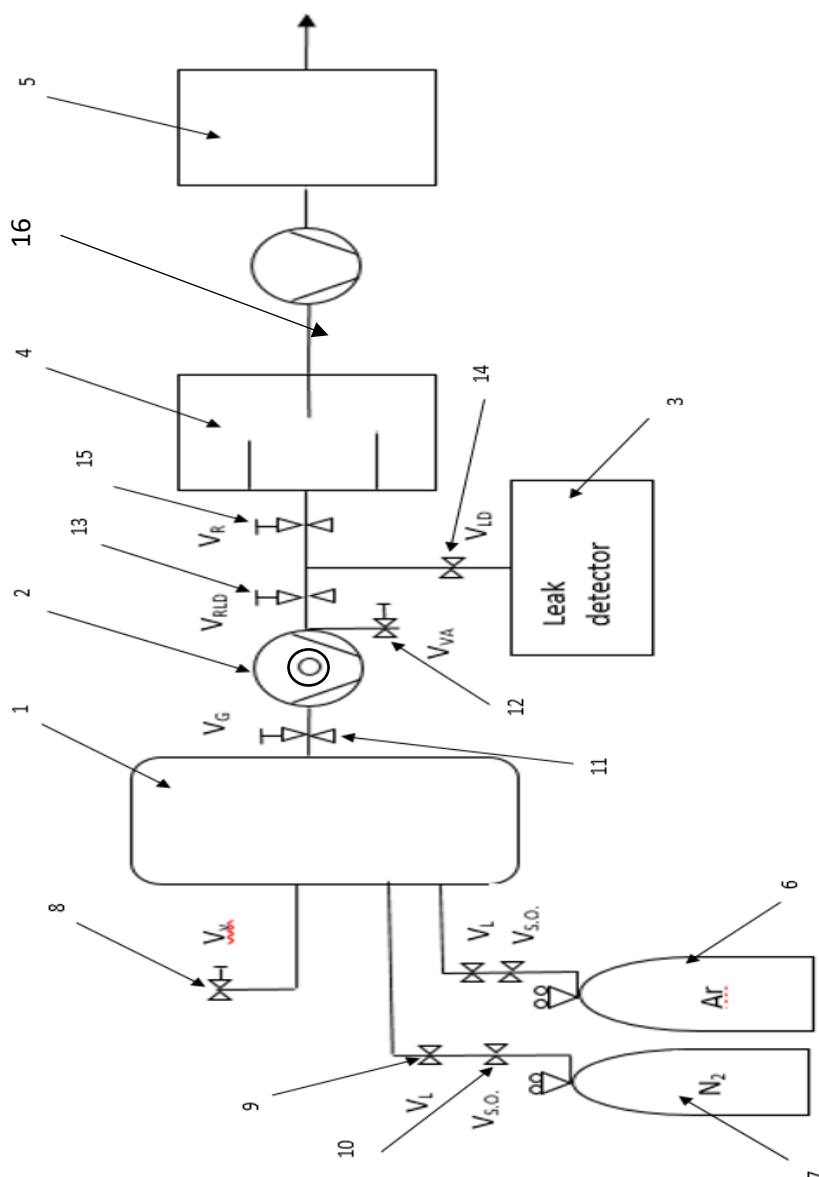
Measuring a system's pressure is the traditional way to classify the degree of vacuum. In the low-vacuum and medium-vacuum range, the number of molecules in a vacuum vessel in the gas phase are large compared to those covering the surface of the vessel. Thus the pumping of the space serves to remove molecules from the gas phase. This vacuum range extends from atmosphere to about 10^{-2} mbar. Many industrial processes that need to outgas or dry materials and components use this region.

The high-vacuum region corresponds to a state where the gas molecules are located mainly on the surfaces of the enclosure and the mean free path equals or exceeds the dimensions of the vacuum vessel. The particles travel in the vacuum enclosure without colliding with other molecules. Thus, in this vacuum region, under these conditions, the pumping consists of evacuating or capturing molecules. The molecules leave the surface and individually reach the pump. This region is extensively used in the preparation and application of vacuum coatings, surface treatment, and modification. This region extends from 10^{-3} to 10^{-7} mbar.

Under ultra-high-vacuum (UHV) conditions, time to form a monolayer is equal to or longer than the usual time for most laboratory measurements (1 second in average). Thus clean surfaces can be prepared and their properties determined before an adsorbed gas layer is formed. This vacuum range extends from about 10^{-7} to 10^{-14} mbar.

3.2. Scheme of sputtering vacuum system

On the Figure 3.1 scheme of sputtering system had been shown.



1 – Vacuum chamber; 2 – Turbo molecular pump; 3 – Leak detector; 4 – Trap for oil; 5 – Filter; 6 – cylinder with Argon ; 7 – cylinder with nitrogen; 8 – Venting valve; 9 – leak valve; 10 – shut off valve; 11 – gate valve ; 12 – automatic ventilation valve ; 13 – rough leak detector valve ; 14 – leak detector valve ; 15 rough valve; 16 – vacuum pump.

Figure 3.1. – Scheme of the sputtering system

In case of vacuum pump 16 it can be used rotary or scroll pump. If the scroll pump has been used, it is not necessary to use trap for oil 4.

It is very necessary in sputtering to obtain pure deposit without some additive molecules.

3.3. Creation of vacuum

3.3.1. Fore vacuum and high vacuum pumping

High-vacuum technology deals with a very wide range of pressure or particle density conditions. Usually, the process of evacuation begins at atmospheric pressure and then proceeds to high or ultra-high vacuum. In a multistage pumping system, the type of pumping mechanism employed is different at atmosphere and at high vacuum. Even if, in principle, a given pumping method could be used throughout the entire pressure range, such an attempt would be impractical in regard to size, weight, or cost of equipment, as illustrated in Figure 3.2.

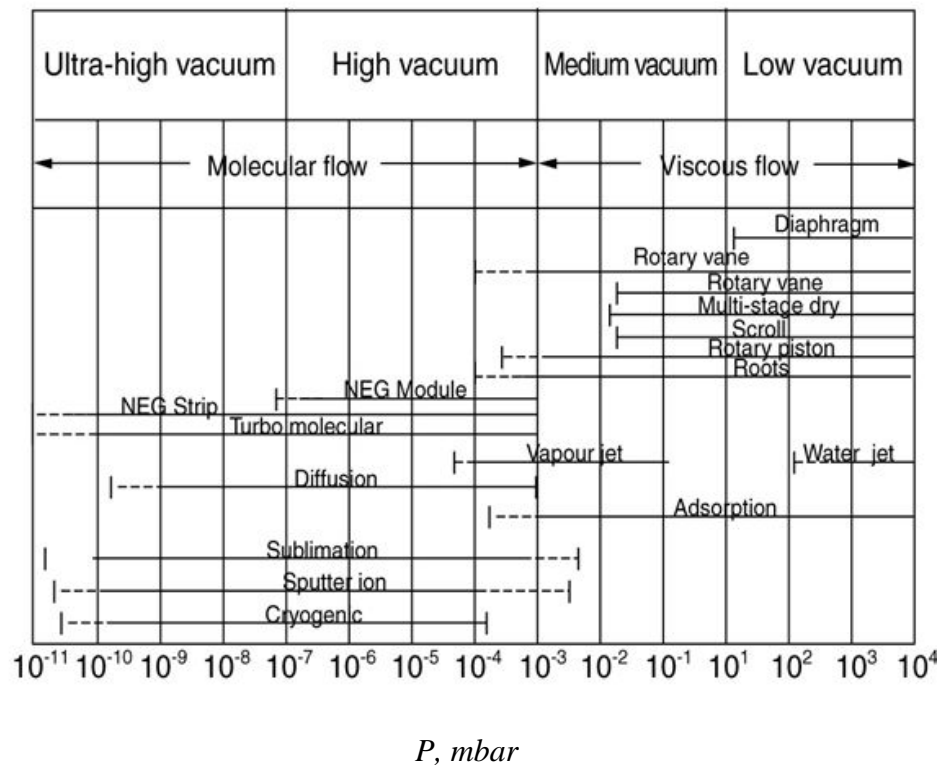


Figure 3.2. – Pressure range, in which the use of various pumps is most economical

The most common pumping arrangement for production of high vacuum consists of a positive displacement mechanical pump for initial evacuation followed by a high-vacuum pump. Often parallel and series arrangements are used. For initial evacuation, the mechanical pumps are used alone, and for obtaining high vacuum, the two types of pumps are connected in series. In such a system, the gas enters the pumping train at high vacuum and is exhausted at atmospheric pressure by the last pump. In some cases, the device may be evacuated and sealed, terminating the pumping process; in others, the pumping is continuously applied to compensate for the gas evolution in the vacuum chamber. In capture pumps (sorption pumps, and particularly in getter-ion pumps), the pumped gas is not exhausted to atmosphere. This has an obvious advantage of isolation from high-pressure environment and the disadvantage of limitation in gas load capacity or the necessity for periodic regeneration or replacement, in the case of getter-ion pumps.

The basic performance of pumps and compressors can be associated with flow and pressure factors. With appropriate allowance for size, power, pumped fluid characteristics, etc., all such devices generally behave according to the pressure flow graph shown in Figure 3.3.

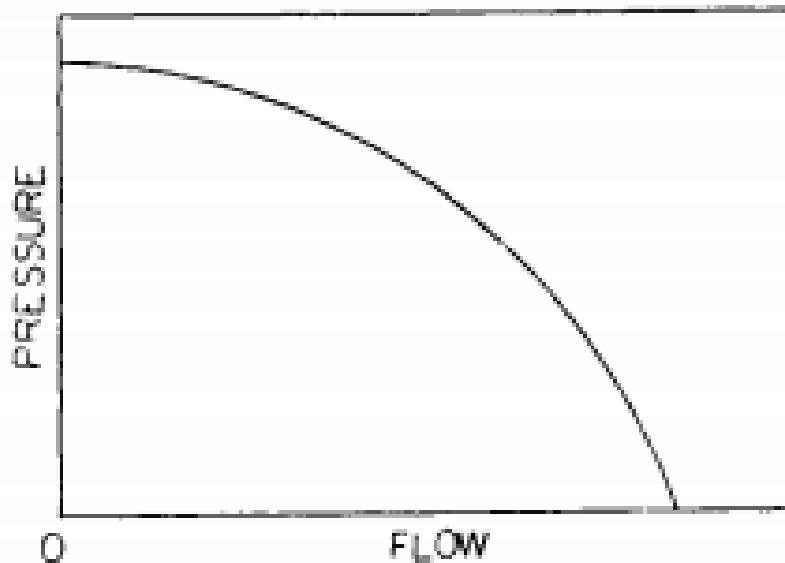


Figure 3.3. - The general qualitative relationship between pressure and flow for most compressors or pumps.

For high-vacuum work, both high-volume flow rate and high-pressure ratio (inlet to discharge) are necessary. The flow rate is associated with the size of the pumping device. Thus, for a given size, the pressure ratio needs to be increased as much as possible. Mechanical vacuum pumps, vapour jet pumps, and turbomolecular pumps produce compression ratios of over 1 million to 1. This can be

compared to industrial plant air compressors, automobile engines, or aircraft compressors not exceeding a compression ratio of 10 to 1. Obviously, high-vacuum pumps require very special designs, and familiarity with their design, construction, operation, and maintenance is an important ingredient of success in producing and using high-vacuum environments.

3.3.2. Mechanical pumps

The development of mechanical pumps was intimately linked with the progress of vacuum science up to the middle of previous century when the introduction of both the sputter ion pump and the sublimation pump provided an alternate method for the production of low pressure. Nevertheless, the mechanical pumps are, with the exception of the sorption pumps, the unavoidable initial stage before any attempt can be made to activate capture pumps and to reach the ultra-high vacuum domain. This is due to their ability to evacuate efficiently from the vacuum vessel the large number of molecules present at atmospheric pressure. However, the limited compression ratio of the pumps limits the achievable ultimate pressure.

In mechanical pumps, the gas present in a vacuum system is transferred from a low pressure to a higher pressure region. In order to be efficient, the pump has to provide simultaneously a finite pumping speed and compression.

To carry out this double task two main mechanisms have been used up to now:

- Isolation and subsequent compression of a gas volume defining a first category often named “Positive-displacement pumps”.
- Transfer to the gas molecules of a preferential velocity direction introducing a mean drift of the gas towards the high pressure region. This category is known as: “Momentum transfer pumps”.

Displacement pumps

The principle of these pumps is next. During a cycle, a given volume of gas at low pressure is trapped mechanically and subsequently compressed to the exhaust pressure.

During this cyclic process two difficulties arise:

- The swept volume has to be sealed in order to ensure a good compression ratio hence an efficient dynamic seal has to be provided.
- The compression of the gas during the pumping cycle creates heat, which must be evacuated.

These two difficulties can be efficiently mastered by the use of a fluid, which produces a sealing film between the moving and fixed parts of the volume while efficiently evacuating the heat liberated during the gas compression. This role was played by water or mercury in the first mechanical pumps but oil now replaces it in a very efficient way.

In order to avoid the presence of oil and the related maintenance and back streaming problems, dry pumps have been developed. Here the absence of an efficient dynamic seal reduces the compression per stage of the pumps and the necessity to evacuate the heat implies the use of an external water cooling circuit. Several successive elementary stages are often combined in dry pumps to improve their compression ratio and to allow gas exhaust at atmospheric pressure.

Oil-sealed pumps

In all these pumps, the compression is produced between one fixed cylinder and a second one rotating off-centred inside the fixed cylinder. The two main types are the piston pump and the rotary-vane pump. Both are able to exhaust gas at atmospheric pressure and their typical main characteristics are presented in Table 3.1.

Table 3.1 - Main characteristics of oil-sealed pumps

TYPE	ULTIMATE VACUUM (Total pressure) (Pa)	PUMPING SPEED (m ³ /h)
Rotary-piston pump	1	30→1500
Rotary-vane pump (single stage)	1	1→300
Rotary-vane pump (double stage)	$2 \cdot 10^{-2}$	1→300

The rotary-vane pump is mainly used for small to medium pumping speed, and is the most commonly used forevacuum pump in accelerators. The rotary-piston pump is often reserved for applications where high throughput is needed, in which case water cooling is necessary. The compression ratio of double-stage rotary-vane pumps can be very high (10 to 8 for air) and their ultimate pressure correspondingly low provided special care is taken. When these pumps operate close to their ultimate pressure, i.e. in the molecular flow regime, the risk of oil-vapor backstreaming is important.

Dry pumps

Despite the very important role played by the oil in the operation of displacement pumps, its presence has two major inconveniences:

- Interaction of the pumped gases, often aggressive in the case of the semiconductor industry, degrades the oil and necessitates frequent oil changes even in the case of the expensive fluorinated oils. This results in excessively high maintenance costs for oil pumps exposed to aggressive chemicals.
- Oil vapor present in the foreline pipe when the pump operates close to its ultimate pressure can contaminate sensitive equipment to which the pump is connected.

Even worse, if the pump stops under uncontrolled conditions this can lead, if the internal safety valves of the pump do not operate, to an important oil migration towards the vacuum system.

For these two reasons the leading market for vacuum technology, the semiconductor industry, has forced the vacuum manufacturers to develop oil-free pumps.

The elimination of oil in the displacement pumps introduces major constraints on the design of the pump: the sealing and the lubrication effects of the oil are eliminated and heat transfer from the mobile parts is much reduced. This results in a reduced compression-per-stage of the pumps and the need for external cooling. In consequence, most of the dry pumps available on the market need water cooling and have more stages (about double) than an equivalent oil-sealed pump. The various types of commercially available dry pumps are summarised in Table 3.2.

Table 3.2 - Various types of dry pumps

Type of pump	Compression per stage	Speed (m ³ /h)	Ultimate pressure
Piston	15-20	12	3-4 Stages, atm → 4 Pa
Diaphragm	200	0.8 → 5	atm → 200 Pa
Scroll	10 ⁵	15 → 600	atm → 1 Pa
Roots	30	25 → 1000	4 Stages, atm → 0.1 Pa
Screw	30-100	25 → 2500	atm → 1 Pa
Claw	20-50	25 → 500	3 Stages, atm → 10 Pa
Tongue/groove	10-20	50	4 Stages, atm → 5 Pa

Different types of pumps are often combined into a single system, e.g. a Roots pump is used to provide high pumping speed at the entrance stage after which claw stages are used to increase the compression at the high-pressure stages where the volume throughput is reduced.

Two types of pump have neither oil nor joints between vacuum and oil: these are the scroll pumps and the diaphragm pumps. The advantage of oil-free pumping is certainly more important for applications where the cost of maintenance is high. In the case of accelerators, the pumping of radioactive zones, where the disposal of contaminated oil and the maintenance of activated pumps is a concern, dry pumps offer an interesting alternative to the oil-sealed type.[2]

3.3.3. Turbo Molecular Pumps

The turbomolecular pump (TMP) invented by Becker in 1957 became commercially available in 1958. Since then it has become very popular in every field of high- and ultra-high-vacuum technique, due to the clean, consistent, and predictable vacuum created, the easy operation, and the advanced degree of operating reliability. The TMP is the only mechanical vacuum pump that together with a roughing pump can attain ultimate pressures in the range below 10^{-10} mbar.

The turbomolecular pump is a bladed turbine that compresses gases by momentum transfer from the rapidly rotating blades of the rotor disks to the gas molecules. The rotor impulse is transmitted to the particles by the superposition of the thermal velocity of colliding particles with the velocity component of the moving rotor surface. The nondirected motion of the particles is changed to a directed motion, creating the pumping process. When the mean free path of the particles is larger than the spacing between rotor and stator blades (molecular flow range, typically $<10^{-3}$ mbar), the action of the rotor is diminished by the frequent collisions between the particles. Therefore, normally, a TMP is not capable of pumping gases against atmospheric pressure and must be backed by an adequate roughing pump.

The pumping speed and the compression of a TMP depend strongly on the rotor geometry and rotational speed. Starting from the 1958 original geometry of the rotor and stator disks, new disk geometries have been developed. These geometries, together with increased rotor speeds, allow much smaller and lighter rotors for the higher-speed range. Because the gas throughput is constant (the product of pressure and pumping speed) in each stage, the blades nearest to the inlet of the TMP are designed to have a high pumping speed and a low compression, whereas the blades nearest to the fore line port are designed for high compression and low pumping speed (Figure 3.4). For economic reasons, it would be impractical to make each stage different from its neighbour. A compromise results in groups of two to four different types of blades, in which each is designed for a particular speed and compression ratio. The methods of manufacturing the rotors and stators influence the pumping speed and compression. Rotors can be made of individually machined disks that are heat-

shrunk to the rotor shaft, by machining complete groups of disks from a single block of material or by manufacturing the rotors using spark erosion. The individually machined disks offer the advantage of making them optically opaque, maximizing them for the compression. The other methods of rotor production yield disks with less opaqueness and lower compression, maximizing them for pumping speed.

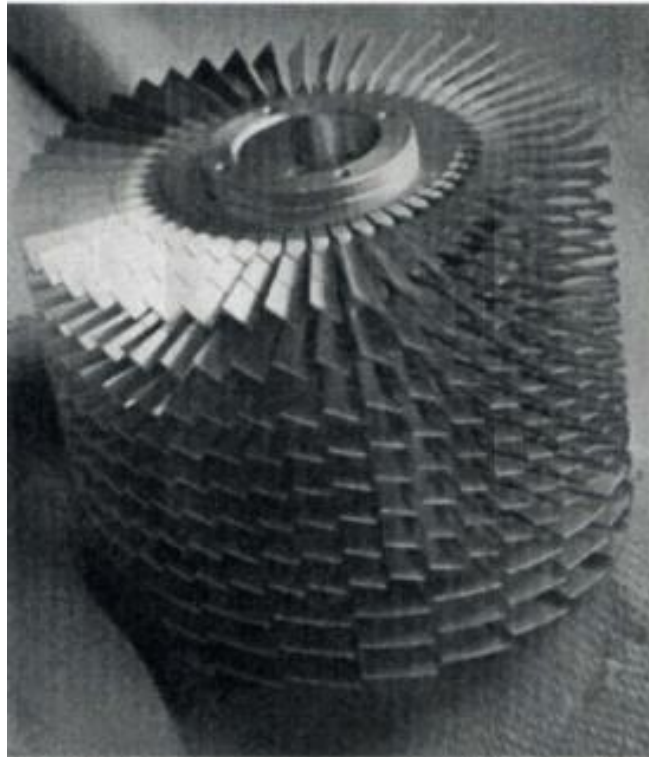


Figure 3.4. – Rotor with different disk design

The stators are either manufactured from individually machined disks or from stampings. The first commercial TMPs were dual-flow ("horizontal") pumps having a double-ended rotor, pumping gas from a central inlet toward both sides and conducting the gas flow in a common foreline. Single-flow ("vertical") TMPs, using single-ended rotors, became available in 1969. The double-ended rotor design allows a more stable bearing design, which is advantageous for easy balancing and lower vibration levels. The single-flow design has little conductance losses between the inlet flange and the rotor, whereas the dual-flow design suffers losses from the inlet to both sides. Today only a few models of commercial TMPs still use the dual-flow design.

3.4. The measurement of low pressure

3.4.1. Overview

The pressures that must be measured in most vacuum systems cover many orders of magnitude. In some simple applications the pressure range may be from atmospheric 10^5 Pa (1000 mbar) to 10^{-3} Pa (10^{-5} mbar) or about 8 orders of magnitude.

These great ranges require more than one gauge to give reasonable measurements. The development of vacuum-measuring instruments (commonly called gauges) over the past 50 years has used transducers (or sensors), which can be classified as either direct reading or indirect reading. Figure 3.5 schematically represents some of the more common gauges.

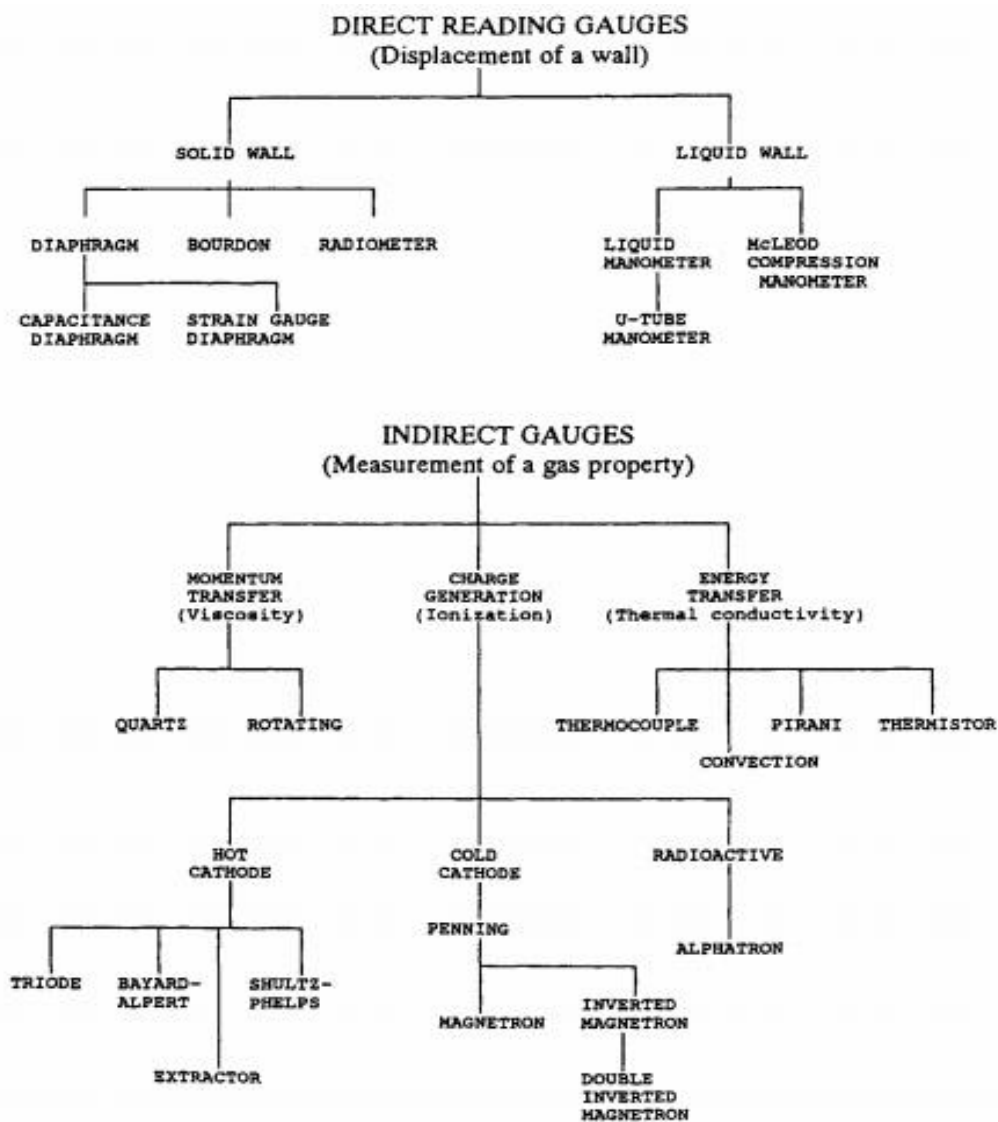


Figure 3.5. - Classification of Pressure Gauges

3.4.2. Indirect reading gauges (Pirani gauge)

The Pirani gauge is perhaps the oldest indirect gauge that is still used today. In operation a sensing filament carrying current and producing heat is surrounded by the gas to be measured.

As the pressure changes, the thermal conductivity changes, thus varying the temperature of the sensing filament. The temperature change causes a change in the resistance of the sensing filament. The sensing filament is usually one leg of a Wheatstone bridge. The bridge may be operated so that the voltage is varied to keep the bridge balanced; i.e., the resistance of the sensing filament is kept constant. This method is called the constant temperature method and is deemed the fastest, most sensitive, and accurate. To reduce the effect of changing ambient temperature, an identical filament sealed off at very low pressure is placed in the leg adjacent to the sensing filament as a balancing resistor. Because of its high thermal resistance coefficient, the filament material is usually a thin tungsten wire; in fact a 10-watt light bulb works quite well (Figure 3.6). A properly designed, compensated Pirani gauge with sensitive circuitry is capable of measuring to 10^{-4} mbar.

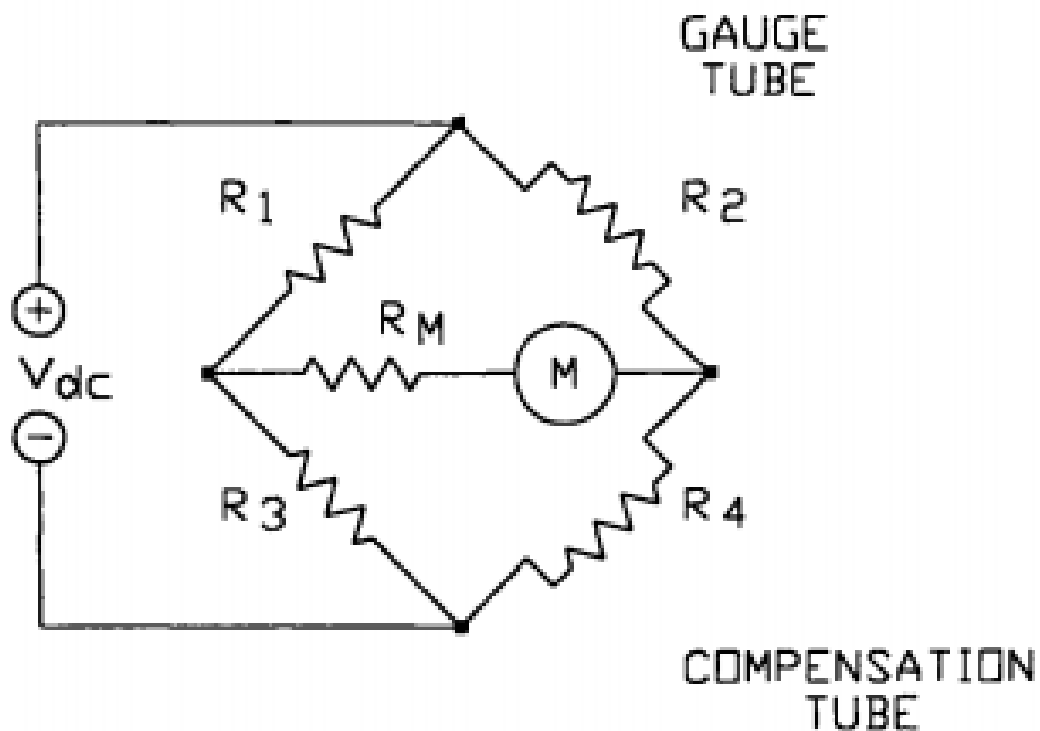


Figure 3.6. - Basic Pirani Gauge Circuit

However, the thermal conductivity of gases varies, which causes a variation in gauge response.

If the composition of the gas is known, use can be made of the calibration curves supplied by the manufacturer. Operation in high partial pressures of organic molecules—oils, for example—is discouraged.

3.4.3. Bayard-Alpert hot cathode ionization gauge

In the 1940s the gauge capable of measuring the lowest pressure was the triode gauge. It soon became apparent that the so-called pressure barrier at 10^{-8} mbar was caused by a failure in measurement rather than pumping. Nottingham correctly deduced that this artificial barrier was caused by electrons striking the grid, causing low-energy X-rays, which in turn struck the ion collector (plate), emitting photoelectrons. The electron emission is indistinguishable from positive ion collection and was calculated to be of the order of 10^{-8} mbar for the triode gauges then in use. In 1950 a simple solution to this problem was proposed by Bayard and Alpert. This is now the most widely used gauge for general UHV measurement. The Bayard-Alpert gauge is essentially a triode gauge reconfigured so that only a small amount of the internally generated X-rays strike the collector. Figure 3.7 shows the essential features of the gauge and a simple circuit.

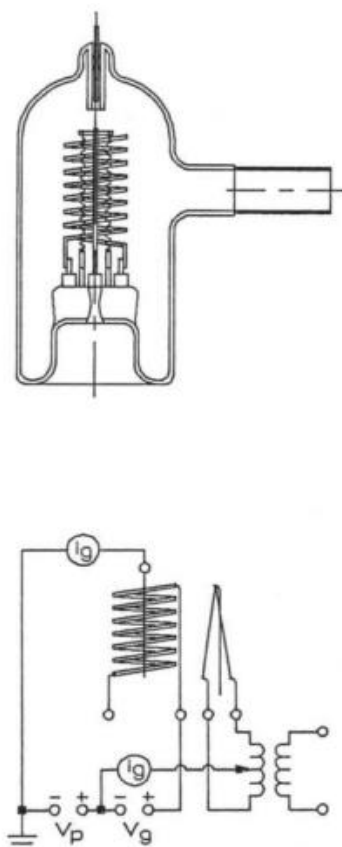


Figure 3.7. - Bayard-Alpert Hot Cathode Ionization Gauge

One can see that the cathode has been replaced by a thin collector located at the center of the grid. The cathode filament is now outside the grid and spaced several millimeters from it. One advantage to the Bayard-Alpert design was its ability to use the same controller as the triode gauge taking into account any sensitivity differences. The nude version of the Bayard-Alpert gauge is shown in Figure 3.8.

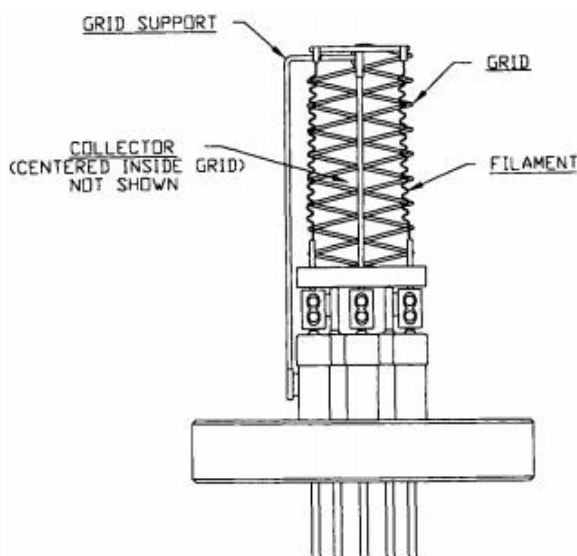


Figure 3.8. - Nude Ionization Gauge

At about the same time the Bayard-Alpert gauge was gaining popularity, Weinriech offered a solution to the burnout of the tungsten filaments then prevalent [29,30]. The use of platinum metals coated with refractory oxides allowed the gauge to withstand sudden exposure to atmosphere with the filament hot. The common combinations used are either thoria or yttria on iridium. It was soon noticed that Bayard-Alpert and even triode gauges of identical structure and dimensions but with different filaments, e.g. tungsten vs. thoria iridium, had different sensitivities, tungsten filament versions being 20 to 40% more sensitive than the iridium of the same construction.

3.4.4. Capacitance diaphragm gauge

Direct reading gauges can be divided into those that use a liquid wall and those that use a solid wall. In either case the gauge measures the pressure by reading the force exerted on a surface by thermally agitated molecules and atoms. Capacitance diaphragm gauge uses solid walls.

If compensated capsule or diaphragm mechanisms are married to suitable electronic measuring circuits, increased performance is achieved. One such arrangement is the capacitance diaphragm gauge (capacitance manometer).

Figure 3.9 shows the salient features of the capacitance diaphragm gauge.

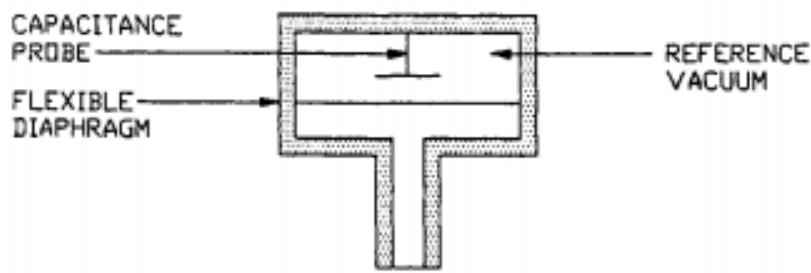


Figure 3.9. – Capacitance diaphragm gauge

A flexible diaphragm forms one plate of a capacitor, and a fixed probe the other. A change in pressure deforms the flexible diaphragm that changes the capacitance, which is converted to a pressure reading. The sensitivity, repeatability, and simplicity of this gauge enables this type of direct reading gauge to be used with appropriate heads as a standard from 10^{-6} mbar to atmospheric pressure. A dynamic range of four or five orders of magnitude is obtainable in a single head. [7]

3.5. Polycold gas chiller

The Polycold® Gas Chillers cool compressed dry gases, such as nitrogen, argon or air, from ambient to cryogenic temperature without pre-cooling. PGC Gas Chillers are closed-loop refrigeration systems that cool a non-recirculating gas stream using a refrigerant to gas tube-in-tube heat exchanger.

Using the Polycold auto-refrigerating cascade technique with a mixed refrigerant, PGC Gas Chillers enable to cool dry gas, which will lead to decreasing the pressure inside the system. Cooled gas inside the Polycold cascade will absorb water vapours from the walls of the vacuum chamber.

PGC Gas Chillers can be also used in thermal testing of electronics, cold gas venting of vacuum chambers, rheology, and low-temperature characterization of materials. They are the most cost-effective systems available for cooling a gas stream in an ultra-low temperature range (-75° to -125°C / -103° to -193°F / 198 to 148 K) without the cost, risk or inconvenience of liquid nitrogen.

Chapter 4

Niobium deposition onto 6 GHz cavities

4.1. Introduction

Building of 6 GHz cavities can be a great solution of performing high number of RF measurements and decreasing research budget. Of course, small 6 GHz cavities will never be comparable to a large cavity, but, on the other hand, this samples are easy to handle, they are ‘real’ cavities and it is great solution for laboratory research work.

They are made from larger cavities fabrication remaining material by spinning technology, they don’t need to be welded. Instead of no less than 1 week RF measurement for the big 1,3 – 1,5 GHz cavities, small 6 GHz cavities in general need 1 day for one RF test.

With small 6 GHz cavities it is much more easy to held traditional and innovative surface treatment and to perform RF tests on a large amount of cavities with a research budget much lower than the one, that is necessary to treat and test real big cavities. It is possible to study such surface treatment technologies like: mechanical polishing, chemical polishing, Nb thin film sputtering, Pd thin film sputtering, thermal treatment etc.

4.2. Methodology of Nb deposition onto the copper 6 GHz cavities

The main aim of this researching work is to divide the optimal parameters of Niobium sputtering onto 6 GHz cavities. During this work vacuum sputtering system and RF measuring system were used.

The order of operation of Nb deposition 6GHz copper cavities:

1. Nb cathode is fixed to the special cavity holder. Niobium rod is used as the cathode in sputtering (Figure 4.1.).



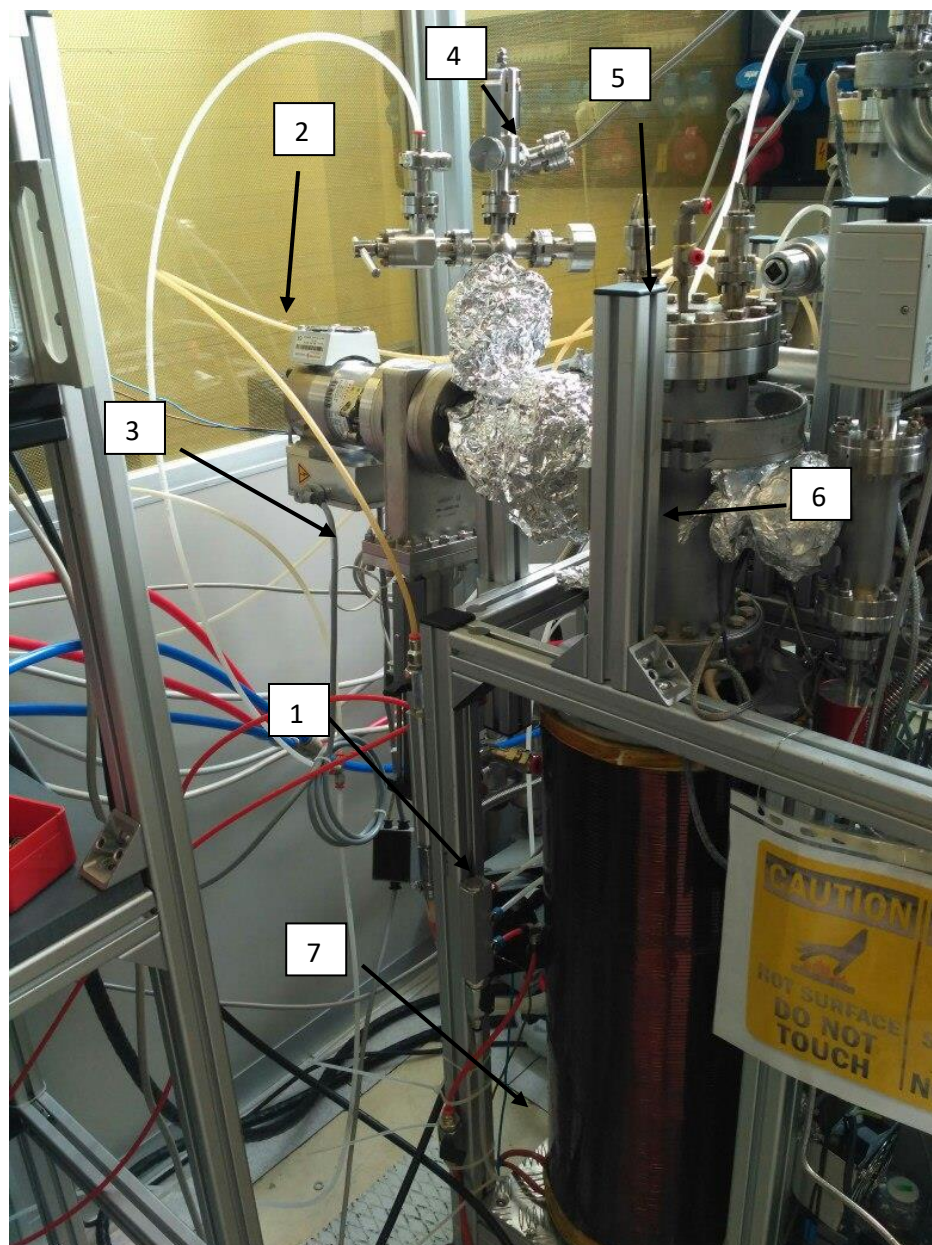
Figure 4.1. – Connected Nb cathode to the cavity holder.

2. 6 GHz cavity is connected to the cavity holder (Figure 4.2).



Figure 4.2. – Connected cavity to the cavity holder.

3. Thermocouple type K is fixed to the center of the cell of the cavity. Two welded to each other wires of alumel and chromel are used like a thermocouple in order to measure temperature of the cavity inside the system (Figure 4.3.).



1 – rotary pump; 2 – turbo molecular pump; 3 – gate valve; 4 – Argon leak valve and inlet line; 5 – cathode holder; 6 – vacuum chamber; 7 – copper coil (cylindrical magnetron).

Figure 4.3. – Sputtering system of Nb deposits onto 6 GHz copper cavities.

4. The chamber 6 is closed.
5. Gate valve 3 is opened.
6. The system is pumped. The rotary pump 1 is started first. After decreasing pressure to $5 \cdot 10^{-1}$ mbar the turbo molecular pump 2 is started.
7. At the pressure of the system $1 \cdot 10^{-4}$ mbar the baking of the system is started. This process is held in order to delete adsorbed gases and water vapors on the walls of the chamber and to decrease outgassing as much as possible. Baking is started at the low pressure in order to prevent oxidation of the system, that can stay in the system at the high pressure. In order to prevent

deformation of the Viton ring of the gate valve the system is divided on the three heating zones (Figure 4.4.). In different zones the temperature of baking is different in order not to exceed Viton maximum deformational point. In zone 1 the temperature is 120 °C and in zones 2 and 3 the temperature of baking is 150 °C.

Baking of the system is being held minimum 24 hours.

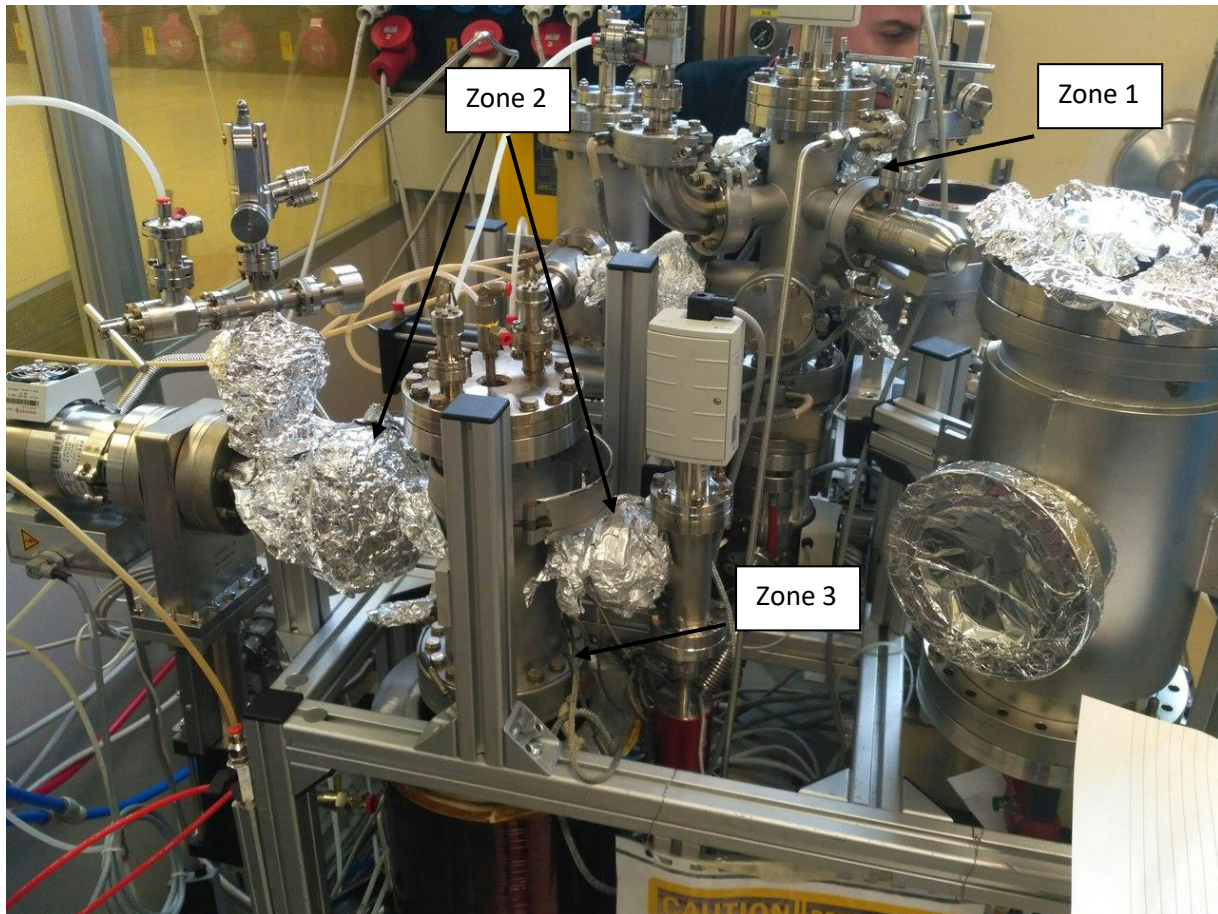


Figure 4.4. – Baking zones of the sputtering system.

8. The process of sputtering is held. Before starting sputtering Nb onto 6 GHz cavity turbo molecular pump should be switched on in “Standby” regime. This procedure prevents heating of the pump under influence of high Argon gas flux. The next step is connecting the wires of the power supply to the chamber. In this case Nb rod is connected as the cathode and chamber is grounded. The water cooling tubes are connected in order to cool down the cathode. After this the leak valve 4, that is connected to the Argon cylinder, is opened until the pressure is increased for $5 \cdot 10^{-2}$ mbar. The next step is switching on the IR lamp, that is placed inside the vacuum chamber, in order to reach the working temperature of the process (550 °C). In the end, the sputtering process is started. Sputtering of Nb film is held at 1 A. Program of time of sputtering is chosen due to the thickness and number of layers of Nb deposits. Time of sputtering can be from 30 minutes to 5 hours.

9. After the end of sputtering the IR lamp is switched off.
10. The turbo molecular pump is switched to the working regime. The system is pumped until the temperature of the system will decrease to the room temperature.
11. After that the gate valve is closed. The turbo molecular and the rotary pumps are switched off.
12. The system is vented.
13. After disconnecting the power supply wires and water cooling tubes from the cavity holder the chamber is opened.
14. The cavity is disconnected from the cavity holder.
15. After that, the cavity should be measured in cryostat. In order to perform these measurements, cavity should be fixed in the special cavity stand. Fixing cavity in the bottom part of the stand is carried out in the clean room with use of special clothes and gloves (Figure 4.5.).



Figure 4.5. – Bottom part of the cavity stand.

16. Next step is connecting the bottom part of the stand to the leak detector (Figure 4.6). After this it is checked on the presence of the leak. In case of a leak the cavity should be reassemble to the bottom part of the cryostat holder.



Figure 4.6. – Leak detection of the bottom part of the stand.

17. The next step is connecting the bottom part to the upper part of the stand.
18. After that cavity stand is pumped to the pressure, lower than $1 \cdot 10^{-7}$ mbar.
19. Cavity stand is checked on presence of leaks by the leak detector (Figure 4.7.). It is well known, that Helium lighter, then Oxygen. Due to exact definition of the leak, checking is hold from upper part of the stand to the bottom part.

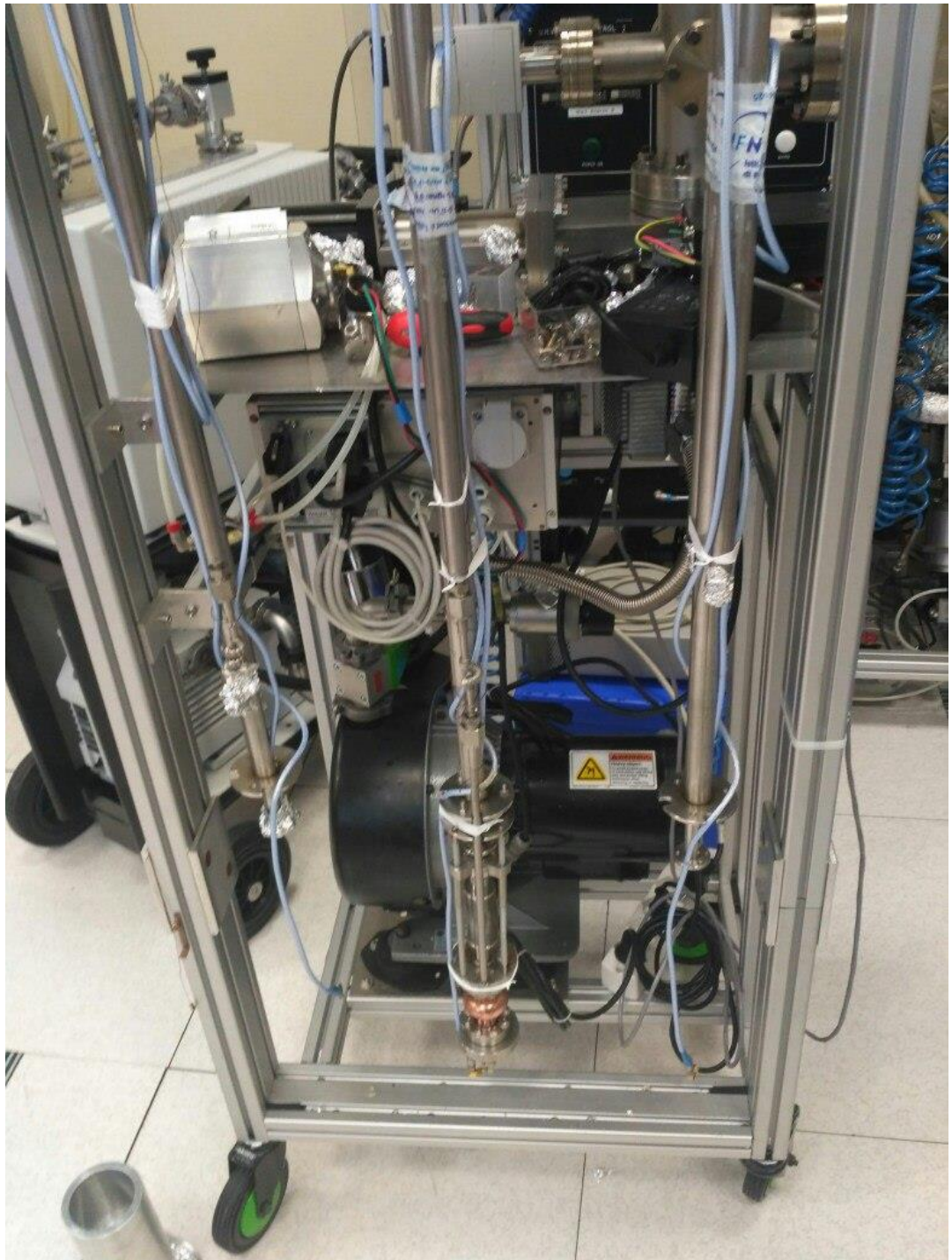


Figure 4.7. – Leak detection of the cavity stand.

20. After that the stand is assembled into the cryostat (Figure 4.8.).
21. Before inserting into cryostat, stand must be pumped.
22. All the RF cables, motor cables and thermometers are connected.

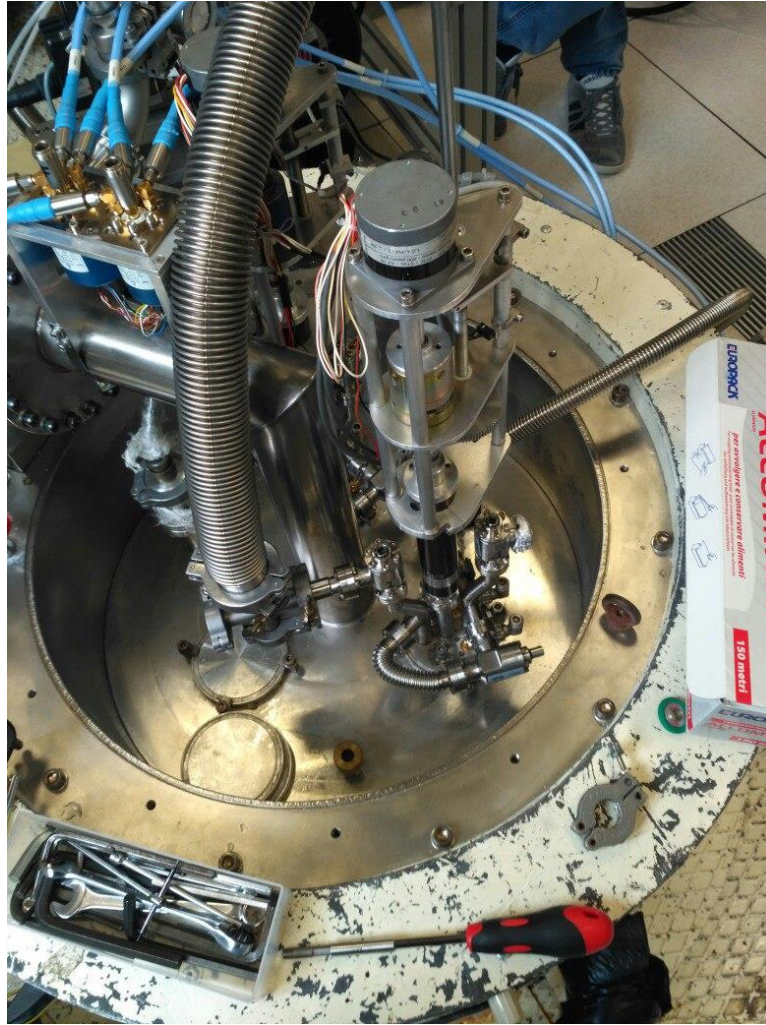


Figure 4.8. – Assembling cavity stand into the cryostat.

23. RF measurements are held for obtaining $Q = f(E_{acc})$ dependence. In order to do that it is injected power through the forward line down to the coupler antenna and then from the pick-up antenna the transmitted power is sent back to the RF software. In the end of measurements, it is obtained a plot of quality factor(Q) versus accelerating field(E_{acc}). Cryostat measurements are normally held at 4.2 K and 1.8 K.
24. During the measurements it is also obtained the temperature, pressure and radiation dependences from the time.
25. Post measurements baking. After holding the measurements, the quality of the deposit is evaluated. In case of bad quality additional baking is held. Cavity is connected to another cavity holder. After that the chamber of additional baking (Figure 4.9.) is closed and pumped. Baking is held at the temperature 120 – 150 °C for 24 hours. It is held in order to remove impurities from the Nb deposit. The next step is holding measurements of the additional baked cavity.



Figure 4.9. – IR lamp in the chamber for additional baking.

26. In the end the cavity is disconnected from the stand.

4.3. Nb magnetron sputtering onto 6 GHz cavities

As magnetic field generator in this system is used cylindrical DC coil, that is made of isolated copper wires (Figure 4.10.). Cylindrical magnetron was chosen due to the shape of the cavity. In case of cylindrical magnetron magnetic field, that is produced by the coil, is parallel to the Nb cathode. Electric field, that is perpendicular to the magnetic field, forces electrons to move circular around cathode. Because of this sputtering occurs.

It was experimentally backgrounded, that the most efficient current of the coil is 10 A ($B = 830$ Ga). In case of higher current coil start to heat because of increasing of the voltage and it is impossible to hold the working coil during the whole time of experiment. On the other hand, using of the lower current doesn't allow to provide sputtering at all. Magnetic field, that is produced by the coil, using low current, is or too low, to provide sputtering, or it is obtained Nb deposit with very low quality.



Figure 4.10. – Cylindrical coil of the Nb sputtering system onto 6 GHz cavities.

4.4. Experimental part

Experiment #1

During the experiment, the cavity was sputtered for 233 minutes at the current 1 A. Nb deposit is multilayer of thickness 40 000 nm (80 layers 500 nm each). Pressure of sputtering is 5×10^{-2} mbar. Before sputtering operations: baking for 84 hours at 600 °C. During RF measurements were obtained next $Q = f(E_{acc})$ dependence (Figure 4.11.). Temperature, pressure and radiation dependences from

the time during cryostat measurements of the experiment # 1 has been shown on the Figures 4.12. – 4.13.

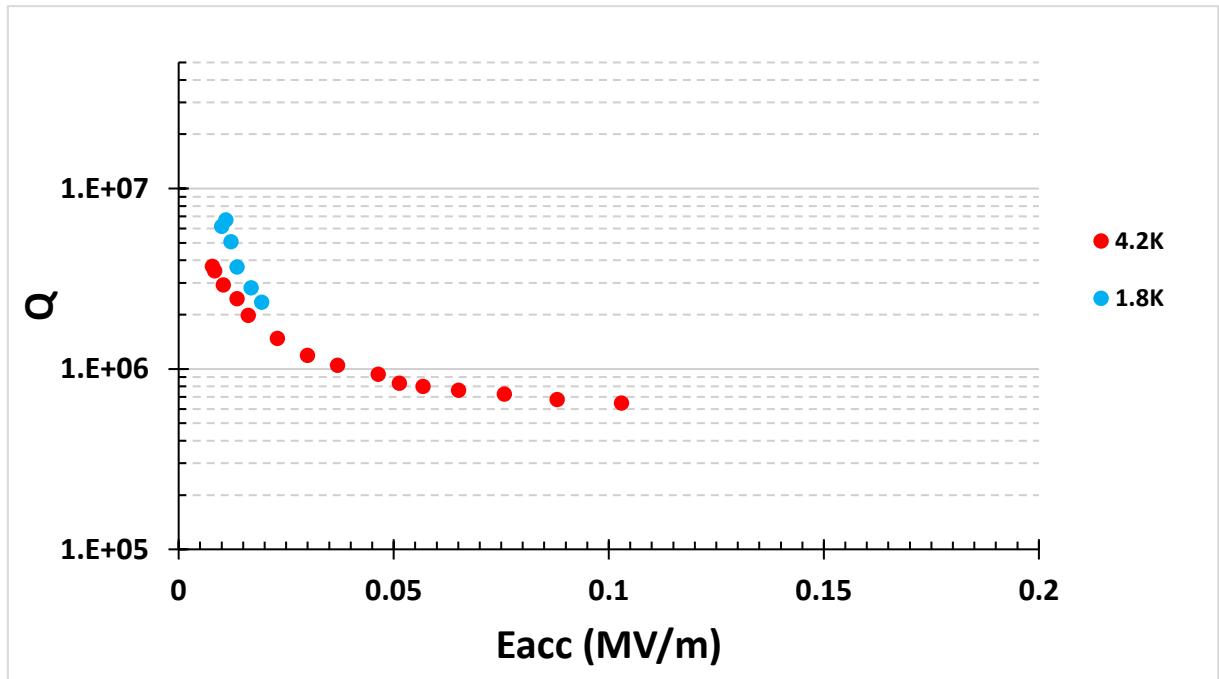


Figure 4.11. – Dependence of the quality factor from the energy of accelerating field, that was obtained during measurements at 4.2 K and 1.8 K.

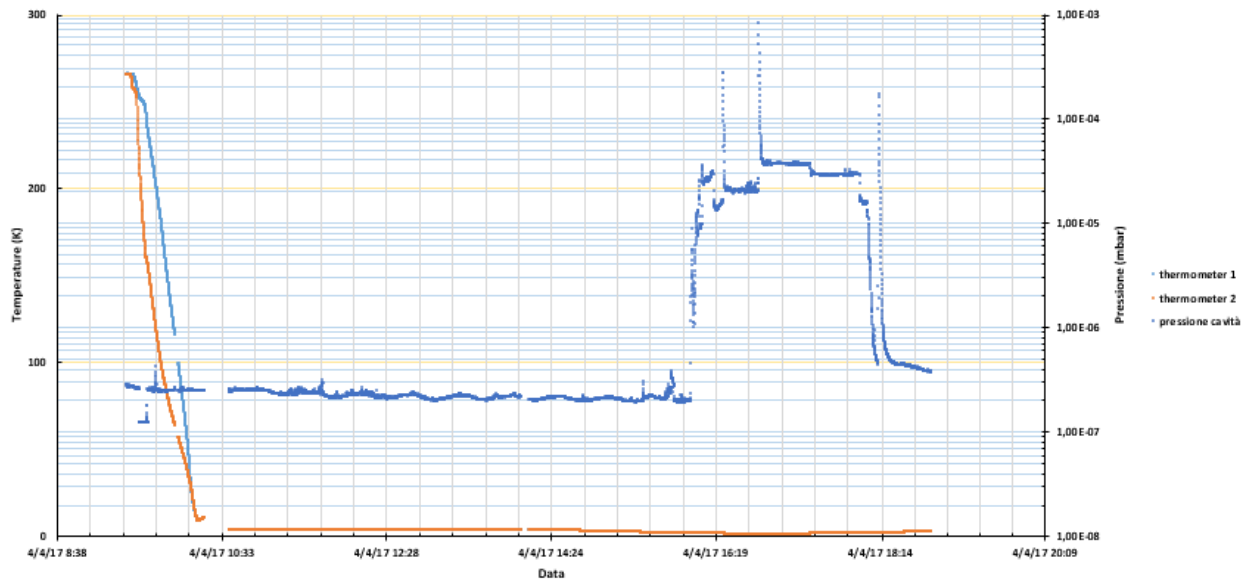


Figure 4.12. – Temperature and pressure dependence from the time during cryostat measurements of the experiment # 1.

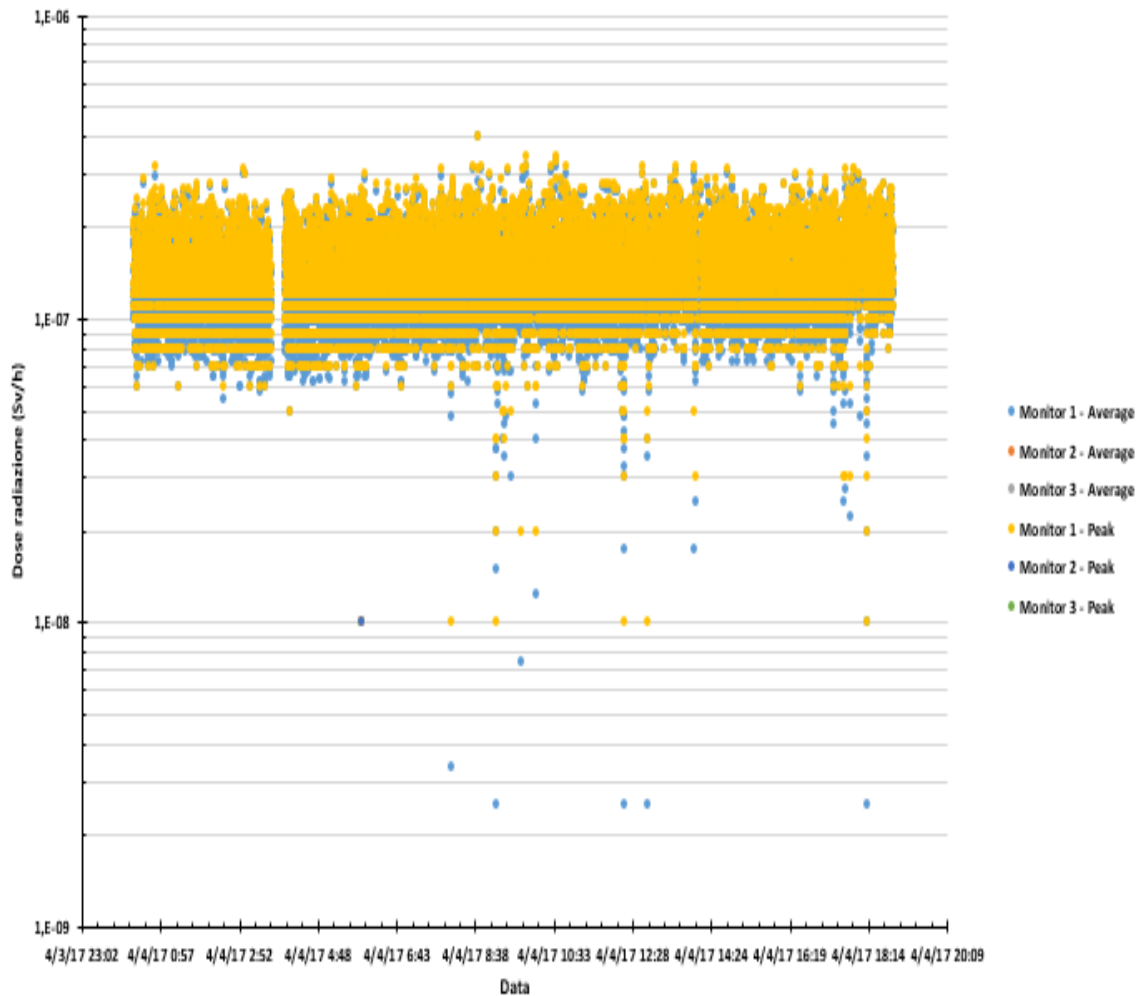


Figure 4.13. – Radiation dependence from the time during cryostat measurements of the experiment # 1.

On the figure 4.11. it is being shown Q-slope of the measured cavity at 4.2 and 1.8 K. As it can be noticed, shape of the slope is not straight, which means, that Nb deposit has not very good quality. On the figure 4.13. it is shown, that during cryostat measurements there was no radiation emission.

Experiment # 2

During the experiment, the cavity was sputtered for 430 minutes at the current 1 A. Nb deposit is monolayer of thickness 100 000 nm. Pressure of sputtering is 7×10^{-3} mbar. Before sputtering operations: baking for 62 hours at 600 °C. After sputtering operations: BCP chemical treatment (in order to remove thin Nb layer) – 5 minutes, first baking for 115 hours at 100 °C, second baking for 24 hours at 120 °C. During RF measurements were obtained next $Q = f(E_{acc})$ dependence (Figure 4.14.).

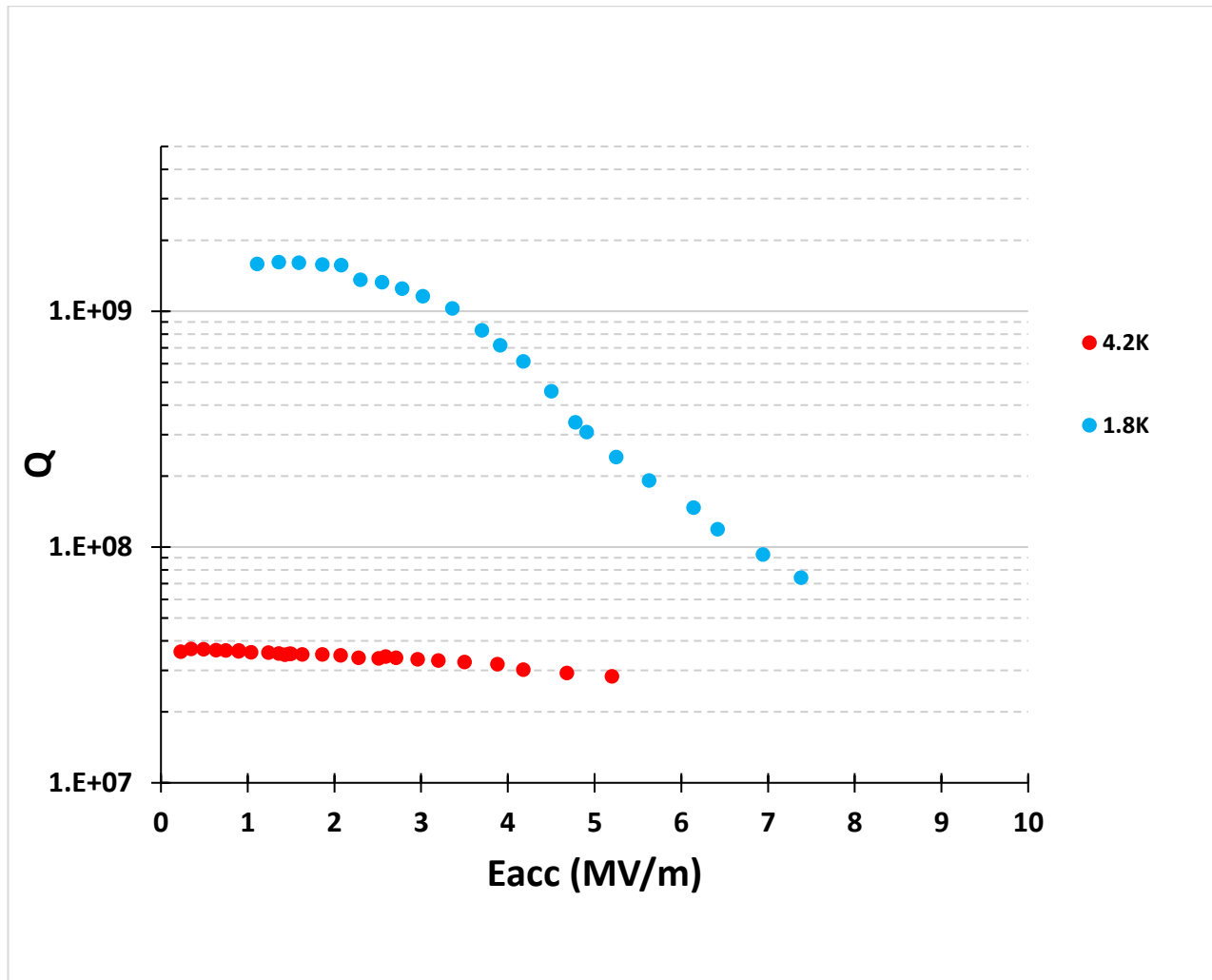


Figure 4.14. – Dependence of the quality factor from the energy of accelerating field, that was obtained during measurements at 4.2 K and 1.8 K at the experiment #2 after all after sputtering operations.

Experiment # 3

During the experiment, the cavity was sputtered for 410 minutes at the current 1 A. Nb deposit is multilayer of thickness 70 000 nm (140 layers 500 nm each). Pressure of sputtering is 5×10^{-2} mbar. Before sputtering operations: baking for 192 hours at 600 °C. During RF measurements were obtained next $Q = f(E_{acc})$ dependence (Figure 4.15.).

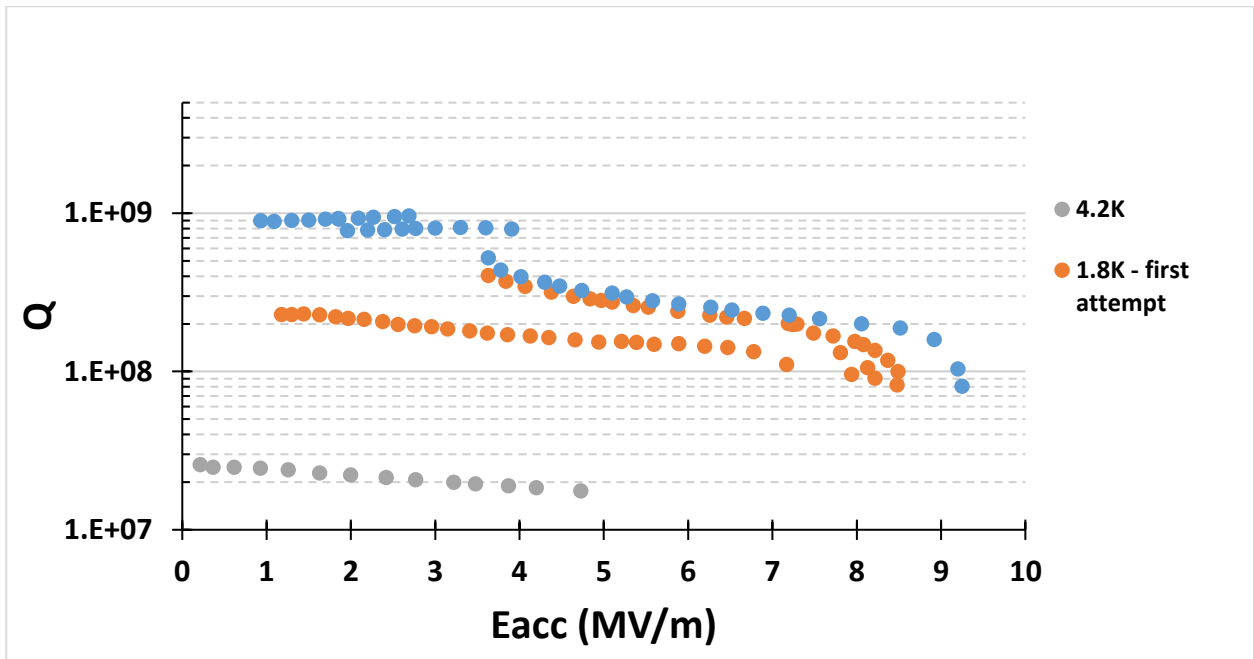


Figure 4.15. – Dependence of the quality factor from the energy of accelerating field, that was obtained during measurements at 4.2 K and 1.8 K at the experiment #3.

After sputtering operation: baking for 10 hours at 600 °C. During RF measurements after additional baking were obtained next $Q = f(E_{acc})$ dependence (Figure 4.16.).

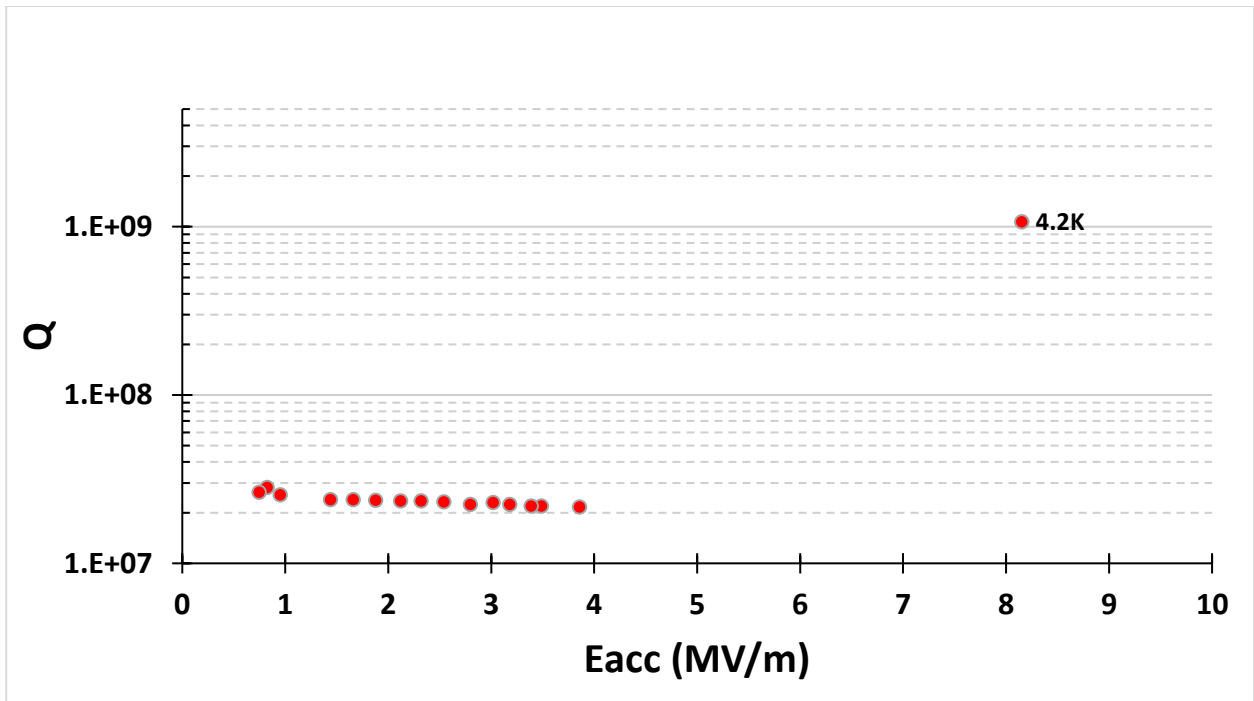


Figure 4.16. – Dependence of the quality factor from the energy of accelerating field, that was obtained during second measurements at 4.2 K at the experiment #3

After sputtering operation: baking for 40 minutes at 730 °C. During RF measurements after second additional baking were obtained next $Q = f(E_{acc})$ dependence (Figure 4.17.).

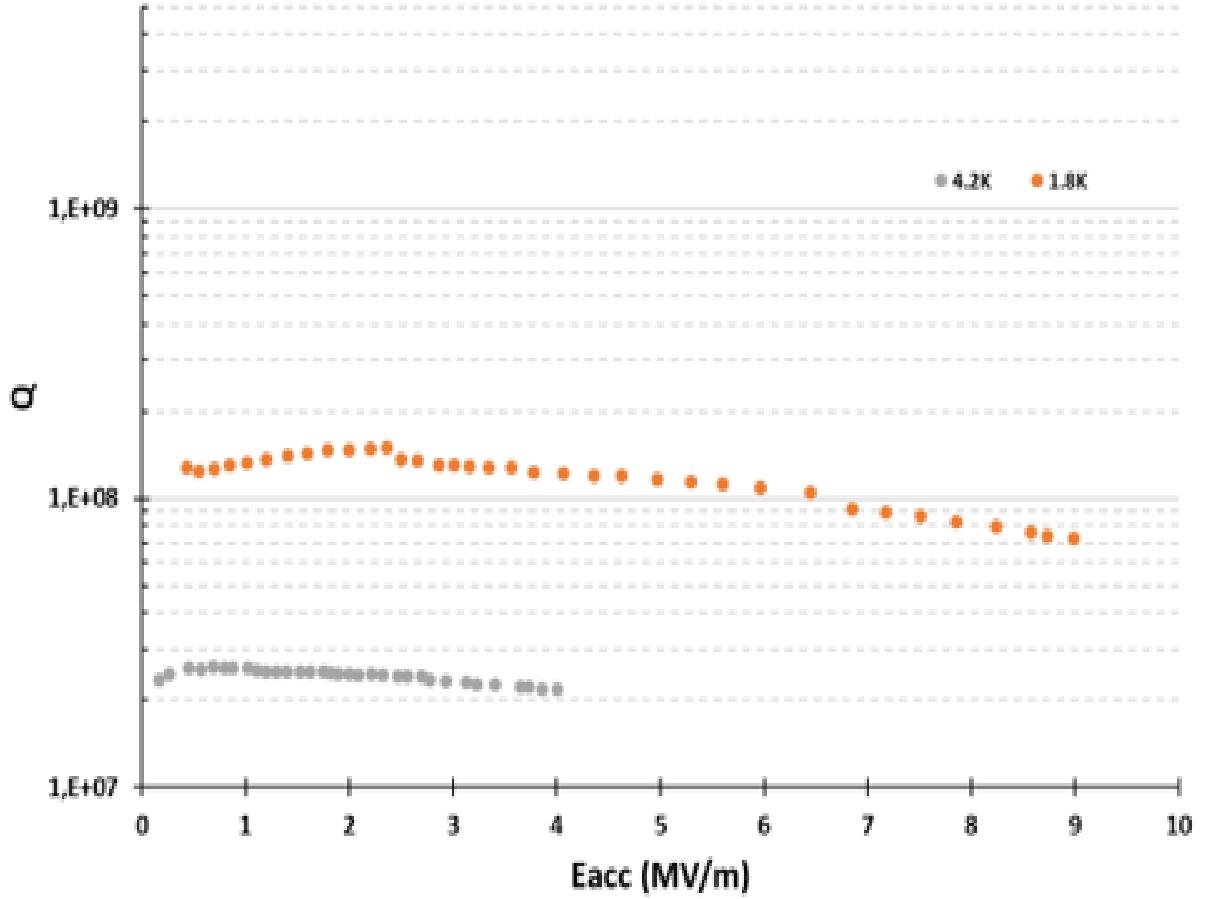


Figure 4.17. – Dependence of the quality factor from the energy of accelerating field, that was obtained during third measurements at 1.8 K and 4.2 K at the experiment #3.

Experiment # 4

During the experiment, the cavity was sputtered for 430 minutes at the current 1 A. Nb deposit is monolayer of thickness 100 000 nm. Pressure of sputtering is 7×10^{-3} mbar. Before sputtering operations: baking for 84 hours at 600 °C. During RF measurements were obtained next $Q = f(E_{acc})$ dependence (Figure 4.18.).

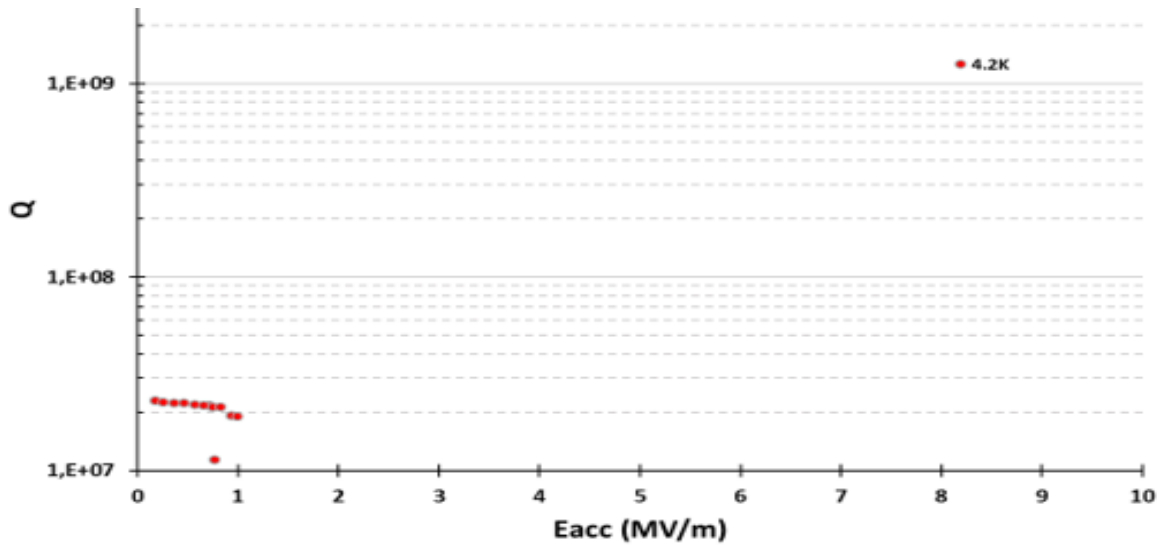


Figure 4.18. – Dependence of the quality factor from the energy of accelerating field, that was obtained during measurements at 4.2 K at the experiment #4.

Experiment # 5

During the experiment, the cavity was sputtered for 375 minutes at the current 1 A. Nb deposit is multilayer of thickness 69 800 nm (161 layer 400 nm each and the last layer 5000 nm). Pressure of sputtering is 5×10^{-2} mbar. Before sputtering operations: baking for 60 hours at 600 °C. During RF measurements were obtained next $Q = f(E_{acc})$ dependence (Figure 4.19.).

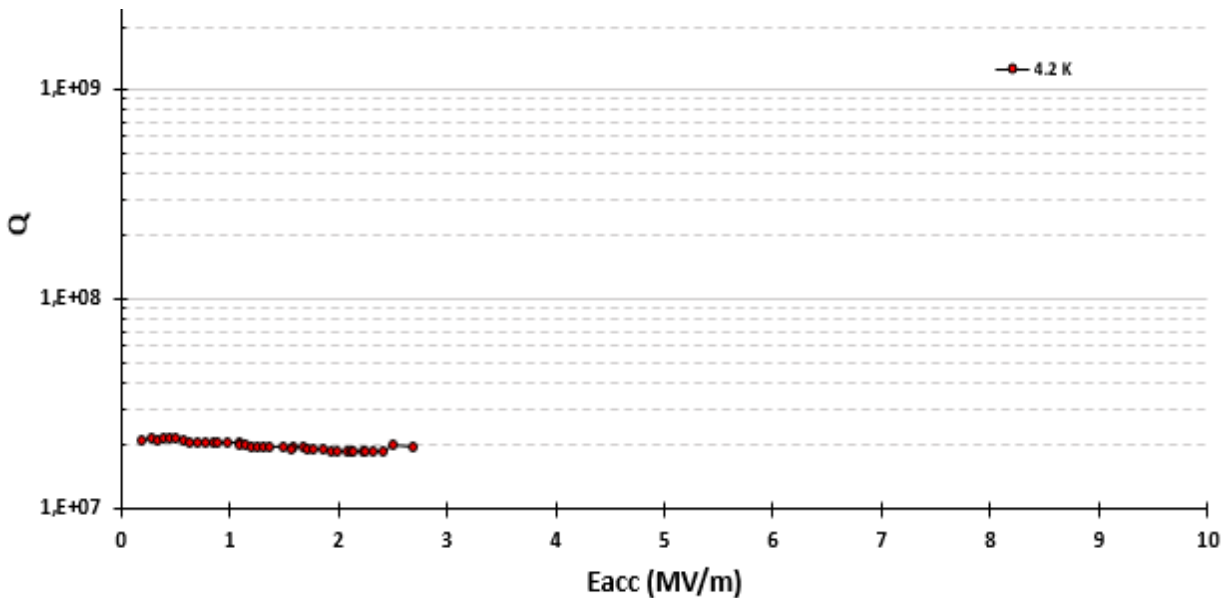


Figure 4.19. – Dependence of the quality factor from the energy of accelerating field, that was obtained during measurements at 4.2 K at the experiment #5.

Experiment # 6

During the experiment, the cavity was sputtered for 430 minutes at the current 1 A. Nb deposit is monolayer of thickness 100 000 nm. Pressure of sputtering is 7×10^{-3} mbar. Before sputtering operations: baking for 61 hours at 600 °C. After sputtering operations: BCP chemical treatment (in order to remove thin Nb layer) – 2 minutes, first baking for 37 hours at 120 °C. During RF measurements were obtained next $Q = f(E_{acc})$ dependence (Figure 4.20.).

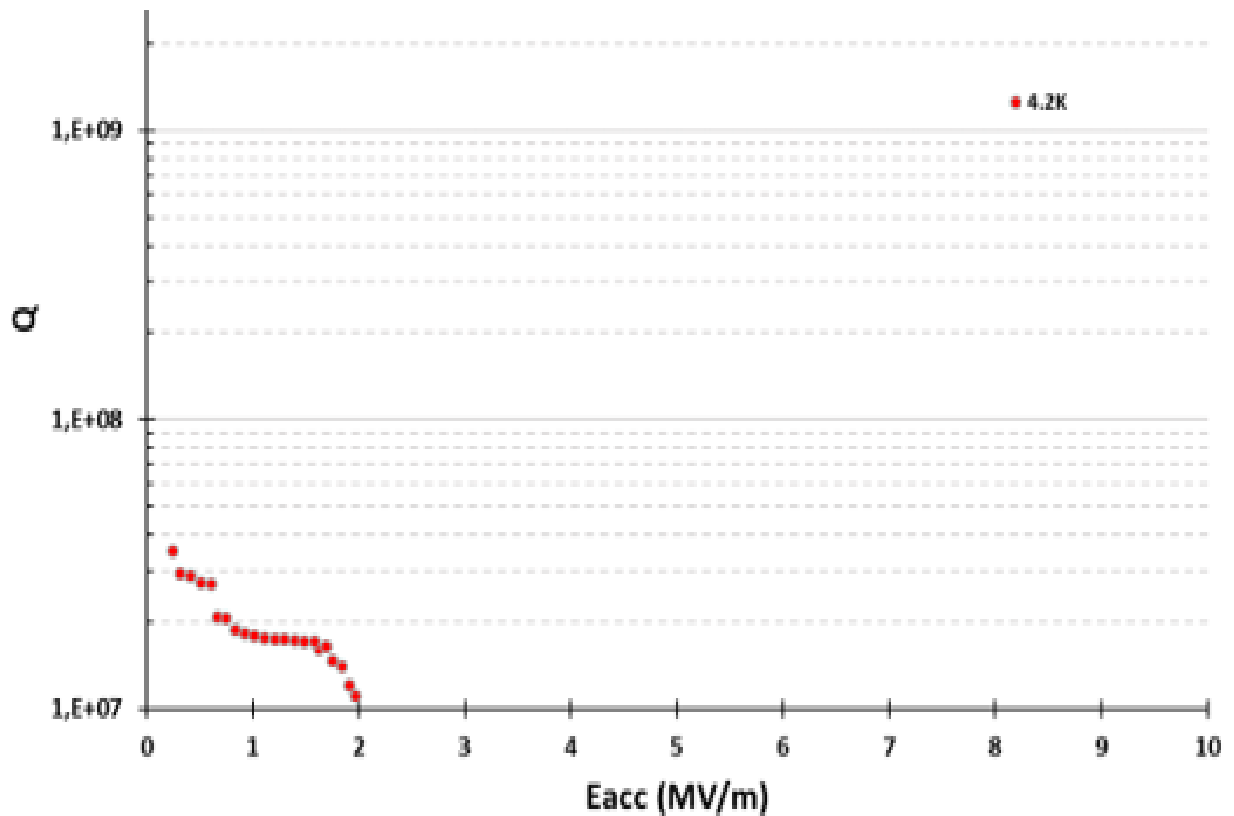


Figure 4.20. – Dependence of the quality factor from the energy of accelerating field, that was obtained during measurements at 4.2 K at the experiment #6.

Parameters of all the experiments, that had been done in this part of research work, is being shown in the table 4.1.

Table 4.1. - Parameters of the Nb coating deposition onto 6 GHz copper cavities

Experiment			1	2	3	4	5	6
Pre sputtering preparation	Time	hours	84	62	192	84	60	61
	Temperature	$^{\circ}\text{C}$	600	600	600	600	600	600
Parameters of the sputtering process	Time	minutes	233	430	410	430	375	
	Current	A	1	1	1	1	1	1
	Coating thickness	nm	40 000 80 layers per 500 nm	100 000 monolayer	70 000 140 layers per 500 nm	100 000 monolayer	69 800 161 layer 400 nm; last one – 5000	100 000 monolayer
	Pressure	mbar	5×10^{-2}	7×10^{-2}	5×10^{-2}	7×10^{-3}	5×10^{-2}	7×10^{-3}
	Temperature	$^{\circ}\text{C}$	550	550	550	550	550	550
After sputtering preparation	BCP chemical treatment		-	5 min.	-	-	-	2 min.
	First additional baking		-	115 hours (100°C)	10 hours (600°C)	-	-	37 hours (120°C)
	Second additional baking		-	24 hours (120°C)	0,66 hour (730°C)	-	-	-

4.5. Conclusion to the chapter

To conclude it is important to say that after preparation, sputtering and holding cryostat measurements the best results of the being done experiments are in the experiment # 3 at the third measurements in cryostat. In this case dependence $Q = f(E_{\text{acc}})$ is the most similar to the line from all made measurements and Q in this case is the highest. The worst result, that was obtained after holding cryostat measurements was in the experiment #1. In this case Q factor was the lowest and $Q = f(E_{\text{acc}})$ was presented as sharp slope. It can be explained by the bad quality of deposited Nb coating or not optimal sputtering parameters of the experiment.

At some cases cryostat measurements weren't held at the temperature 1.8 K. It is connected with opening leaks in the system during reaching Helium λ -point. In that cases during decreasing the temperature the vacuum of the system has been lost and it was impossible to hold the measurements.

Chapter 5

Nb deposition onto Quarter Wave Resonators (QWR)

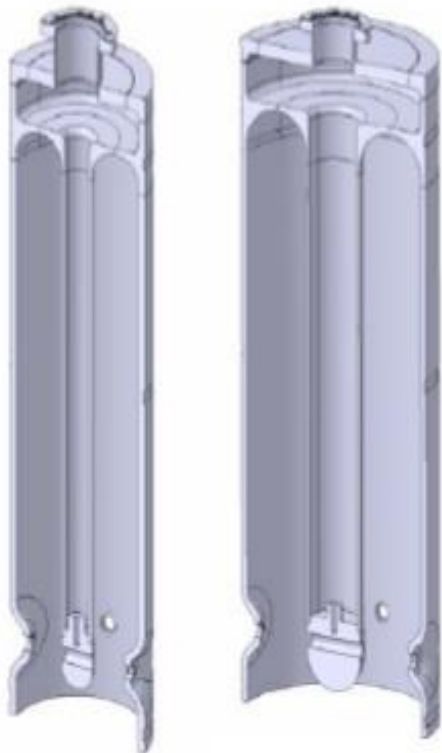
5.1. Introduction

The Quarter Wave resonator is a basic resonant structure that consist of a length of transmission line shorted at one end and “open” at the other end, the length is nearly a quarter of the free space wavelength of the lowest resonator frequency. The high impedance at the open extreme can be used to accelerate the particles, building up high voltages, needed for particle acceleration. The QWR was created in 1981 for heavy ion acceleration.

The main advantages of the QWR are the followings:

1. A broad curve of the transit time factor.
2. A structure which is simple to manufacture and balance electrically.
3. High frequency of the lowest mechanical mode.
4. Low peak surface field values.
5. Efficient cooling of the inner conductor.
6. Elimination of the end plates which are necessary in split loop and spiral resonators and which can be a source of frequency drifts and loss joints.

Mostly, QWRs are used in the acceleration of low velocity ions. These types of cavities can be made using different materials (lead-plated copper, niobium explosively bonded to copper, pure niobium metal and niobium sputtered on cooper). Mostly used are two types of β -type cavities (Figure 5.1.).



Cavity	Low β	high β
No. of Cells	2	2
f (MHz)	101.28	101.28
β_0 (%)	6.3	10.3
Design gradient E_{acc} (MV/m)	6	6
Active length (mm)	195	300
Inner conductor diameter (mm)	50	90
Mechanical length (mm)	215	320
Gap length (mm)	50	85
Beam aperture diameter (mm)	20	20
U/E_{acc}^2 (mJ/(MV/m) ²)	73	207
E_{pk}/E_{acc}	5.4	5.6
H_{pk}/E_{acc} (Oe/MV/m)	80	100.7
R_{sh}/Q (Ω)	564	548
$\Gamma = R_s \cdot Q_0$ (Ω)	23	30.6
Q_0 for 6MV/m at 7W	$3.2 \cdot 10^8$	$5 \cdot 10^8$
TTF max	0.85	0.9
No. of cavities	12	20

Figure 5.1 – Low and high β cavities [3]

5.2. Methodology of preparation of the system for quarter wave resonator sputtering and holding of the Nb sputtering process

The system for QWR sputtering (Figure 5.2) was not used for a long time. In order to prepare the system next steps were made:

1. All electrical connections, copper thermoresistances, heating elements and cables were checked. In order to check correct work of the heating system the quarter wave resonator sputtering system had been heated.



Figure 5.2 – System for QWR sputtering

2. After heating of the system, it was discovered, that one external heating lamp had been burnt during the previous experiment. Next step was replacing old heating lamp onto the new one. Also it was discovered, that ceramic parts, that protect wires and placed inside the chamber, were sputtered. In order to prevent heating of the ceramic protective parts and obtaining of the short circuit inside the chamber sputtered ceramic parts were changed on the unsputtered.
3. After that the system was heated in order to check correct work of heating lamps (Figure 5.3).



Figure 5.3 – Test heating of the system

4. In order to prevent damaging Nb cathode during the sputtering process because of the heating, the water cooling system, equipped with Digital Flow Switch RF2W7, was made (Figure 5.4). Water cooling tubes were connected to the system from the bottom part of the rotated magnetron. During the sputtering process water will circulate in the magnetron and cool down the target.



—————> - water flux inside the tubes

Figure 5.4 – Water cooling system of the magnetron

5. In order to observe movement of plasma during the sputtering process it was decided on the time of experimental test change upper magnetron onto view-port flange. Also heating lamps were dismantled from the system and were not used during the experimental test.
6. Next step was checking the proper work of the magnetron. In order to do that system was closed and pumped without the cavity. Sputtering process was started and movement of Argon plasma had been observed (Figure 5.5).



Figure 5.5 – Argon plasma, that was observed during the sputtering process

7. After providing experimental test upper view-port was replaced on the upper magnetron and heating lamps were assembled into the system.
8. Next step was preparation of the cavity in order to make deposition. First step was chemical treatment of the quarter wave resonator. Chemical treatment was done in order to replace Nb deposit, that was sputtered during previous deposition of Nb onto the QWR.
9. Cavity was placed in the chamber and the chamber was closed. The chamber was covered by the aluminum foil for safety reason. After that the system was baked at 150 °C for 96 hours (Figure 5.6).



Figure 5.6 – Baking of the system

10. The sputtering process was held. Time of the process = 30 minutes, $I = 48\text{ A}$, $U = 280\text{ V}$.
11. In the end the sputtered QWR cavity was placed into the cryostat in order to measure the quality of the Nb deposit.

Parameters of the experiment is being shown in the table 5.2.

Table 5.2 – Parameters of the Nb deposition onto Quarter Wave Resonator.

Process	Parameter	Quantity
Pre sputtering baking	Time, hours	96
	Temperature, °C	150
Sputtering process	Time, minutes	30
	Current, A	48
	Voltage, V	280
	Pressure, mbar	$1 \cdot 10^{-2}$

5.3. Using of magnetron in QWR sputtering system

Niobium deposition.

In order to deposit Nb onto the QWR walls in this sputtering system double - wall cylindrical Nb cathode is being used.

Magnetron sputtering source can be defined as a diode device in which magnetic fields are used to form electron traps which are so configured that the $E \times B$ electron drift currents close themselves along annular closed trajectories.

The construction of the magnetron is based on this principle in order to decrease as much as possible the electron losses and increase the plasma. The magnets are placed on a stainless steel tube to follow closed double spiral path. Because of the particular configuration, the magnets are made of Neodymium Iron Boron that is a magnetic material with high Curie temperature. The magnetic field of this magnets are axially oriented. With this configuration the uniformity should be satisfactory because the magnetron is connected to a motor to rotate during the cavity deposition.

In this system deposition of the uniform coating is being reached by using of a rotated magnetron. Innovative part of this system is being presented by the target, which is not being moved, but the magnetic path is joined to a motor to be rotated during the deposition. In this way it is possible to confine the plasma along the substrate

Pre-sputtering process

After initial evacuation of the atmospheric air, the vacuum must be maintained by pumping the gases produced by the system components; for this reason, has been used getters which are materials able to trap gas molecules to form stable compounds or solid solutions.

Niobium is a powerful getter that can be used to dissolve and trap gases like hydrogen and oxygen and also other light elements like carbon and nitrogen.

A niobium magnetron has been placed on the top of the vacuum chamber in order to be used as a getter pump before the deposition of the film. The pre-sputtering process, using the top niobium magnetron, is being held with parameters: time: 15 min., current: 2 A, voltage: 350 V.

5.4. Conclusion to the chapter

System of niobium sputtering onto the quarter wave resonators had been prepared, checked and tested. The successful attempt of Nb deposition onto QWR had been made.

Innovative using of the rotated cylindrical magnetron increased deposition rate of the vacuum system and considerable decreased time of sputtering process (from several hours to 30 minutes).

The system of the niobium sputtering onto quarter wave resonators is very complicated and is hard to handle. It is needed a team of scientists to work with it. In this chapter was described only start of the work with this system. Full research can take several years and the work was done for 4 months. Nevertheless, the start of work was successful and it can be continued by the perspective investigation.

Chapter 6

Niobium deposition onto TESLA-type 9-cell RF cavities for particle accelerators

6.1. Introduction

The superconducting radio frequency cavities are the fundamental parts of the accelerator structure and a less than revolutionary ideas on Particle Acceleration physics, each new development of future accelerators facilities deal with innovation on superconducting cavity technology.

In the last 20 years, National Institute of Nuclear Physics (INFN), has been mainly working to the R&D on alternative manufacturing techniques for superconducting cavities. Now, if to analyse a standard TESLA-type elliptical 9-cell accelerating cavity, since each resonator weight is around 25 kg (without calculating the scrap material) and niobium has a cost of about 600 €/kg, it is easy to understand that, it is needed to develop a new manufacturing technology, otherwise the Large Hadron Collider at CERN will be the last of the large accelerators. In detail, a bulk Niobium 9 cell cavity costs approximatively 90 k€, considering material, machining and chemical process, for a total of 1.44 G€. However, if we consider the same cavity but produced in OFHC copper with Niobium thin coating, an excess estimation of cost is 15 k€, approximatively a sixth of bulk Niobium cavity, for a total of 0.24 G€. It is easy to understand that if accelerator community want to build a facility like ILC, that has approximatively 16000 9-cell cavities, the use of thin film technology may allow a saving of 1.2 G€.

6.2. Using of the quartz tube as the chamber of the vacuum system.

In order to deposit a good superconductive Niobium thin film, a high vacuum system is required. For this reason, it was built a vacuum chamber and the inductive furnace, taking into account the 9-cell elliptical cavity dimension, maintaining the highest standards of design.

A fundamental component of the vacuum system is the process chamber. In this case, it consists of a quartz tube with internal and external diameters respectively of 240 and 250 mm. The total length is 2000 mm. Quartz is a very particular material due to its mechanical, electrical, thermal, chemical and optical properties. In fact, quartz is a group IV metal oxide, which has good abrasion resistance, electrical insulation and high thermal stability.

During preliminary test, unfortunately the quartz tube cracked on one side due to the sealing configuration (Figure 6.1).



Figure 6.1 – Cracking of the quartz tube

This inconvenient has led to further delay in the study of magnetron source. In fact, two months were necessary for the machining of quartz tube. The tube has been shortened by 200 mm in order to remove the cracked side. In this period, re-design of vacuum tight between quartz and vacuum system has also been carried out. In particular, the aluminum flange fixing quartz tube and guarantee vacuum tight, were machined in order to insert a rubber ring between the aluminum base and the end of the quartz. This configuration avoids the direct contact between metallic flange and SiO_2 tube, so the force exerted by pressure during vacuum production ($\approx 5000 \text{ N}$) is amortized by the O-ring and there is no longer the danger of a crack on the extremity of quartz vacuum chamber. The O-ring is not continuous so it does not generate virtual leaks, the vacuum sealing is always guaranteed by Viton O-ring that presses the quartz externally; Figure 6.2 shows a scheme of this configuration.

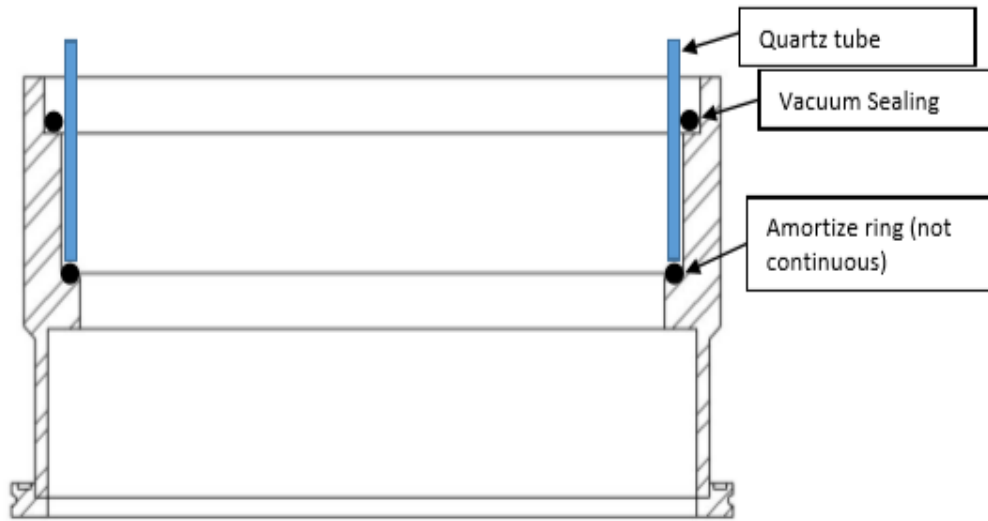


Figure 6.2 – New aluminium flange design

6.3. Outgassing curve of the system

The specific outgassing speed of a system is expressed in terms of quantity of gas per unit time per unit surface, expressed in $(mbar \cdot l) (s \cdot cm^2)/$ and it depends on the kind of material considered and its history. The following procedure has been used to estimate the outgassing rate of the complete system: the pendulum gate valve is closed in order to seal the chamber and the chamber pressure is monitored with time (Figure 6.3). The basic pressure is $5 \cdot 10^{-8}$ mbar. With an inner calculated surface equal to 1.12 m^2 and a volume of 1126 liters, the degassing rate is calculated using:

$$Q_{out} = \frac{dP}{dt} \frac{V}{A} \quad (6.1)$$

The value dP/dt is the pressure speed increasing into the chamber, obtained interpolating linearly the pressure variation with time. Without baking an outgassing rate equal to $1.1 \cdot 10^{-8} (mbar \cdot l) (s \cdot cm^2)/$ is obtained. That value was absolutely not deemed sufficient to obtain high quality superconducting Nb films.

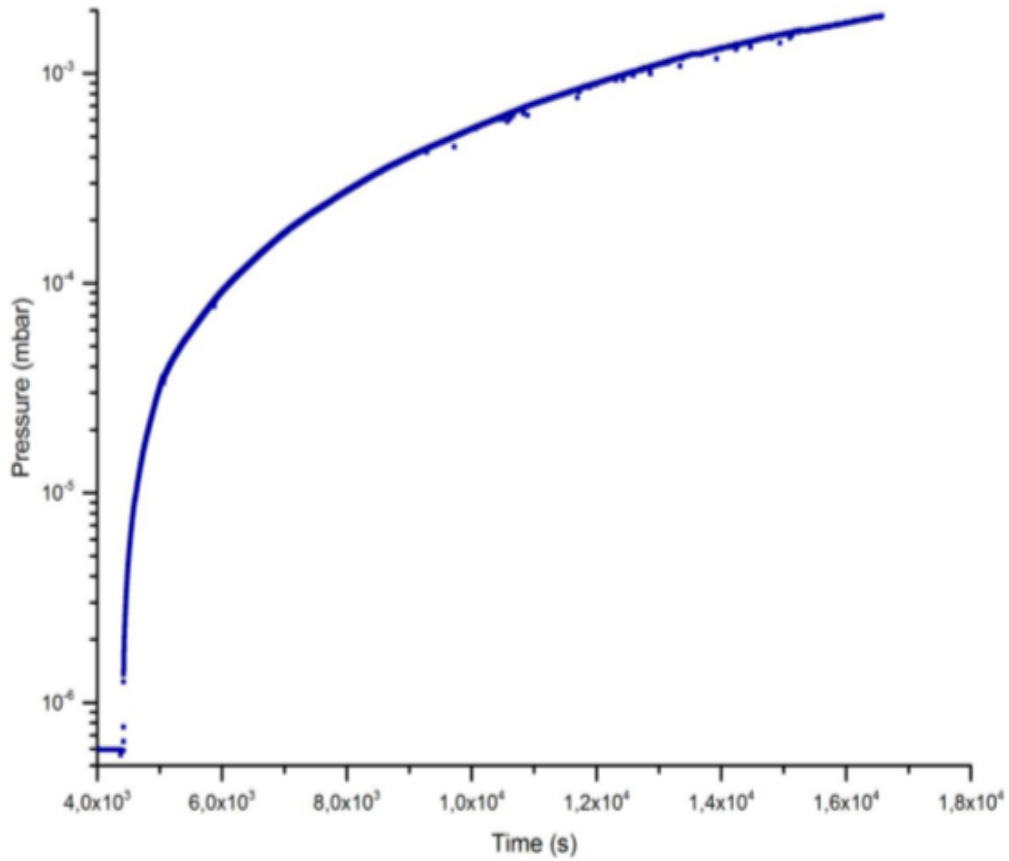


Figure 6.3 – Outgassing curve, obtained without baking.

6.4. First test with quartz shield

Around the cathode 6 GHz cavity, for the first test, a quartz tube is integrated internally to the chamber quartz tube to allow the visual observation of the plasma, avoiding the metallization of the outer quartz tube (Figure 6.4). The whole cathode structure is designed in Niobium. Indeed, the rod supporting the cathode, the support plates, the screws and the 6 GHz cavity is machined using bulk Niobium.

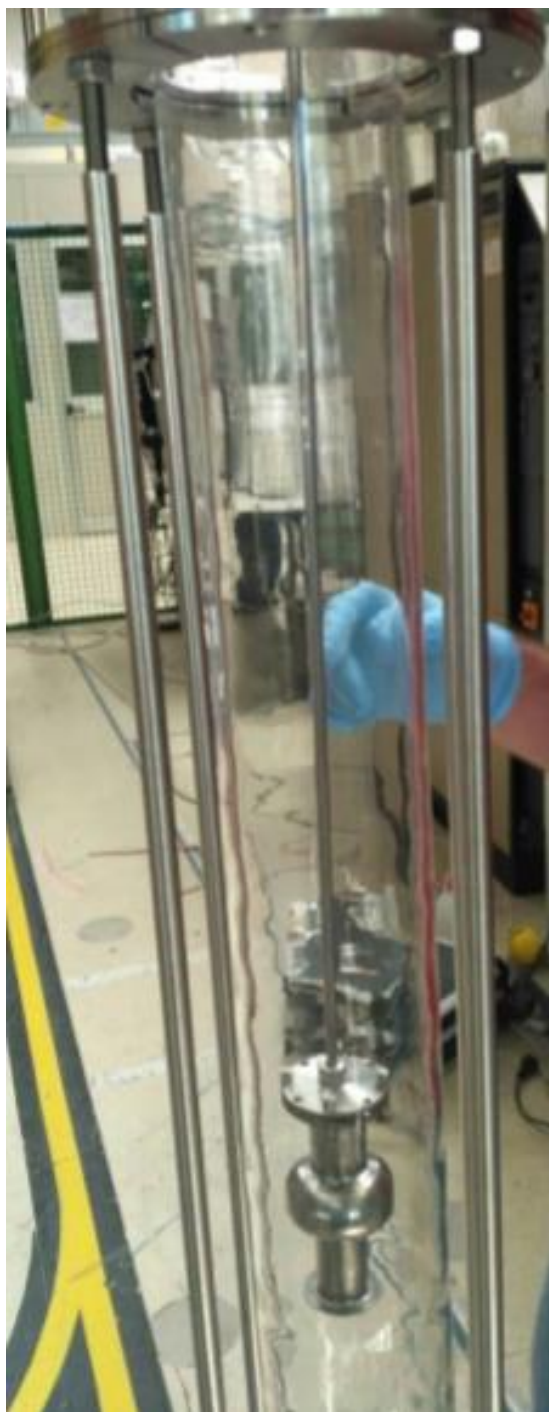


Figure 6.4 - 6 GHz cathode Niobium cavity assembly with quartz shielding

During first test positive results were obtained, in Figure 6.5 is visible the sputtering plasma close to the 6 GHz cavity used as cathode.

The vacuum base pressure before sputtering was $< 4 \cdot 10^{-6} \text{ mbar}$, during the process the Argon pressure was $5 \cdot 10^{-2} \text{ mbar}$. The parameter used during this first test are summarized in the Table 6.1.



Figure 6.5 - Plasma during first sputtering test using 6 GHz cavity as cathode.

Since the number of coils of the inductor is 28 for a total length of 1.6 m, it is possible to calculate the magnetic field starting from Faraday's law of induction that, in a first approximation, the magnetic field axial and internal to the spiral is given by:

$$B = \mu \cdot \frac{N}{\ell} \cdot I \approx 11 \text{ G} \quad (6.2)$$

where N is number of spires for the length ℓ and I the current passing through the solenoid. This magnetic field is sufficient to ignite the plasma and to sputter the Nb cathode but is not so intense in order to promote a good plasma confinement.

Table 6.1 – Sputtering parameters during first test with quartz shield

Parameter	Value
Sputtering tension	418 V
Sputtering current	0,51 A
Sputtering power	210 W
Inductor tension	401 V
Inductor current	48 A
Inductor power	19,2 kW
Inductor frequency	15,6 kHz
Sputtering Ar pressure	$5 \cdot 10^{-2}$ mbar



Figure 6.6 - Sputtered quartz tube after holding of the first test

6.5. Second test with copper shield

Figure 6.9 shows the second setup. A copper tube substitutes the inner quartz tube in order to simulate the cavity design. On the copper tube, some special holes were made in order to accommodate test samples (Figure 6.7). In this way, we can test and measure the magnetron performance coating quartz samples with a dimension of $10 \times 10 \text{ mm}^2$ fixed on the copper tube (Figure 6.8).



Figure 6.7 - Particular of copper tube with holes for holding quartz samples



Figure 6.8 - Quartz samples fixed onto the Cu tube

The wall thickness of the tube is 2 mm, so the magnetic field inside the tube is only ≈ 0.23 G, not enough sufficient to ignite and sustain a sputtering discharge. The introduction of the copper tube will change the inductor parameters (frequency and current) and also the magnetic field strength. Figure 6.9 shows a rendering section of the system assembled. On the centre is visible the Niobium cathode 6 GHz cavity, all around it the copper tube used to simulate the cavity that must be coated.

Figure 6.10 shows the assembly ready to be inserted inside the vacuum system, on the left the whole system with visible the quartz samples, on the right a particular of the centring system of the upper side of the copper tube. The rod visible in the centre of the copper tube is the Nb support of the 6 GHz cavity. The test has 2 objectives: first to establish whether the plasma lights up inside the cavity and second, to analyse the deposition uniformity of the source.

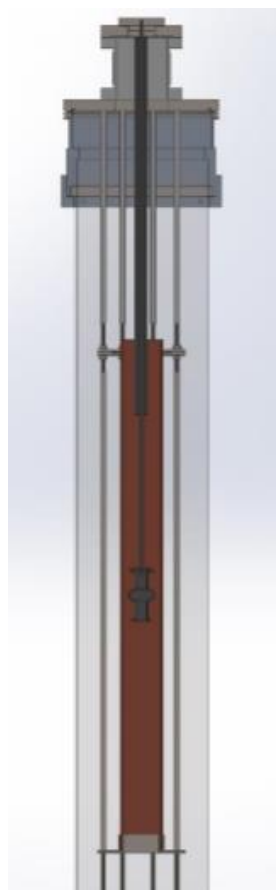


Figure 6.9 - Section of 6 GHz test magnetron simulating the copper cavity.



Figure 6.10 - Left: picture of the copper shield assemblies on the system, on the centre 6 quartz samples are visible. Right: a detail of the upper centring system of the Cu tube.

The vacuum base pressure before sputtering in this test was $< 4 \cdot 10^{-7}$ mbar, during the process the Argon pressure was from $5 \cdot 10^{-2}$ to $2.5 \cdot 10^{-1}$ mbar. The parameters used during this first test are summarised in Table 6.2.

Table 6.2 – Sputtering parameters during second test

Parameter	Value
Sputtering tension	760 V
Sputtering current	0,31 A
Sputtering power	236 W
Inductor tension	380 V
Inductor current	82 A
Inductor power	31,1 kW
Inductor frequency	8 kHz
Sputtering Ar pressure	$0,5 - 2,5 \cdot 10^{-2}$ mbar

Figure 6.11 shows the sputtering process. It is visible the plasma inside the copper chamber from the hole used to fix the samples.



Figure 6.11 - Argon plasma inside the copper tube during sputtering process.

As could be observed from Table 6.2, the inductor current during process is around 82 A and it generates a 18 G magnetic field inside the coil. In this case, with 2 mm Cu thickness the magnetic field close to the magnetron is only 1.16 G, not enough to ignite the plasma.

In fact, the plasma is ignited at high Ar pressure ($\approx 10^{-1}$ mbar) in diode mode, in this test, and the magnetic field is insufficient to confine electrons close to the cathode surface.

Figure 6.11 shows the plasma inside the cavity. Evaluating the results, the plasma starts in diode mode and the intensity was not sufficient for coating the test samples.

6.6. Using of the magnetron in the system for niobium deposition onto TESLA-type 9-cell RF cavities

First solution of the internal magnetron.

Figure 6.12 shows the first sputtering choice, capable to coat a 9-cell cavity simultaneously in each cell. The magnetron structure is composed by nine Nb 6 GHz cavities connected between them by a Niobium tube.

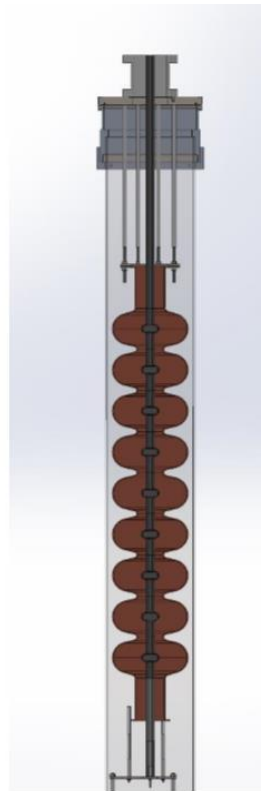


Figure 6.12 - Magnetron optimized for coating 9-cell cavity. The cathode is composed by nine 6 GHz cavities connected by Nb Tube. Eight SS rods support the copper cavity. On the bottom is visible the cavity centring system.

The inductive heating coil generates the magnetic field necessary for sustain the plasma (Figure 6.12). Eight Stainless Steel rods support the copper cavity. The rods have also the possibility to bias

the cavity during the sputtering process. There is no cooling system inside the cathode, in this configuration, due to permanent magnets are not present and Niobium melting temperature is 2468 °C.

Figure 6.13 shows a detailed section of the apparatus. The external inductor coil is visible. It provides the electromagnetic field for heating the copper cavity and the magnet field necessary to sustain the plasma. The inductor is in air, external to the quartz vacuum chamber. On the other side, in vacuum, it is visible the 9-cell copper cavity and the Niobium cathode composed by nine 6 GHz cavities fixed by a Niobium tube. The cathode works at a tension of -800 V and the plasma generated on its surface erodes the niobium for coating the internal surface of the copper cavity.

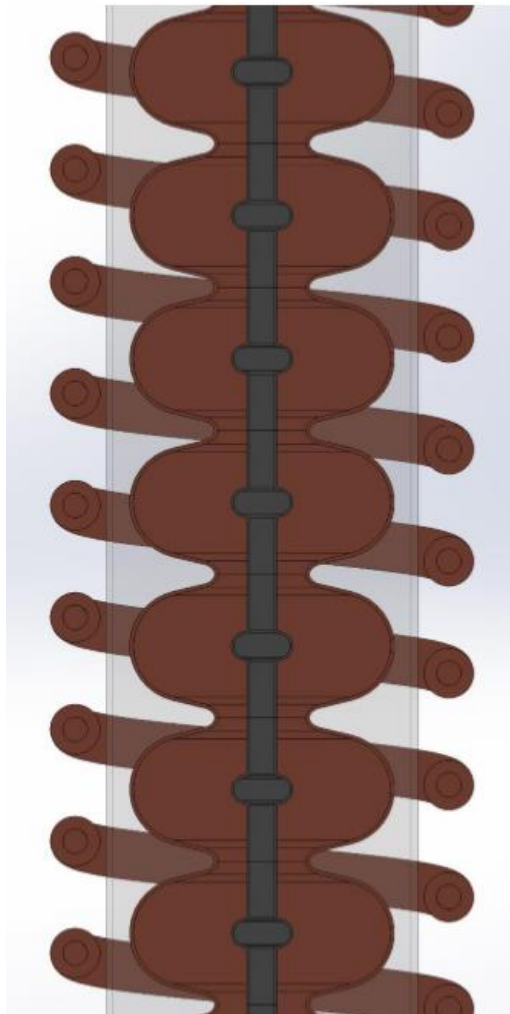


Figure 6.13 - Detail of the magnetron. The spiral of external inductors is visible. Inside the quartz tube is visible the 9-cell copper cavity and the 6 GHz niobium cathode

Second solution of the internal magnetron.

Another possible solution evaluated, consists in a magnetron source composed by rotating magnets.

For this application, it was decided to work on two different cases. The first one consists in generating a “spiral” along the cathode using North-South magnets. The plasma is horizontal on the cavity equator and it is vertical along the cavity cut off. In this way, also the deposition rate is higher on the cavity equator (where there is a higher surface) and lower along the cut off. It is possible to obtain a uniform coating along the cavity and there is only one plasma pattern for all the cells. The magnetic configuration could be produced using permanent NdFeB magnets or a permanent magnetic rubber (Plastimag®) which could be adapted to follow the desired pattern. The advantage of magnetic rubber is the easiness in the source assembly; on the other hand, however, NdFeB magnets have stronger magnetic proprieties and have a higher Curie temperature.

The selected NdFeB permanent magnet is MPN35EH; it was chosen for its high Curie temperature, indeed, it can work until 200 °C, and it has a strong magnetization, up to 1 T. However, ease of assembly given by Plastimag, has an effect on magnetization and Curie temperature, which are almost half, compared to the NdFeB. At the same time, the material used as magnet support is Nylon 6, which has a working temperature between 40 and 100 °C (so compatible with water-cooling), has an excellent mechanical stability and it easy to machine. The Nylon 6 is used a substitute of PVC (used in previous magnetron design) for its higher Tg and for safety reasons, considering case of degradation (i.e. during water cooling fault) in Nylon 6 there is not chlorine inside that could produce dangerous gasses like HCl. In order to allow water cooling of cathode and at the same time rotation, a particular top cathode support was designed. Figure 6.14 shows a rendering of the magnetron top flange. All these components were machine at LNL mechanical workshop. Figure 6.15 shows a picture of the final assembly. From the top is visible the rotating gear, the rotating feedthrough for rotation of the magnets and for water insulation, after that, the special aluminium components designed in order to water cool the magnetron with, visible water tubes already connected.

This structure is assembled on a CF100 flange fixed on a standard CF100 ceramic feedthrough used to insulate the cathode (negative potential) from the ground.

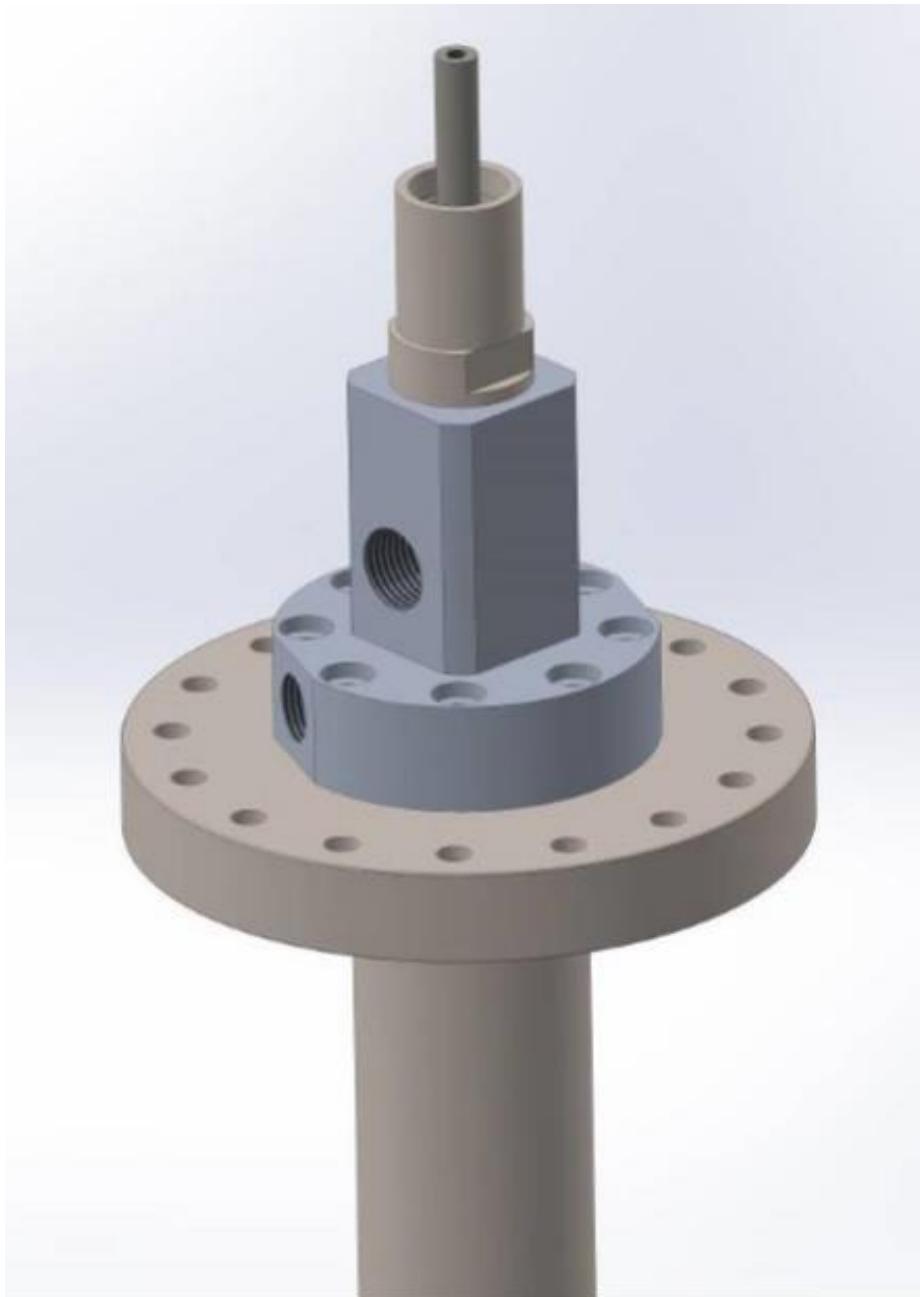


Figure 6.14 - Rendering of the top magnetron flange. From the top is visible the rotating feedthrough that permits rotation of the magnets and at the same time water insulation, after the special aluminium components designed in order to water cool the magnetron.

Figure 6.15 shows a section of the whole sputtering configuration with the rotating magnet. Inside the cavity it is visible the Niobium cathode and inside it, the rotating magnet pack. The top ISO 250 flange is used for supporting the cavity through eight Stainless Steel rods with the possibility to bias it. The cavity is fixed to the rods by a circular centring ring that presses and supports it. The CF100 ceramic insulator that support the magnetron is also fixed to the top ISO 250 flange.

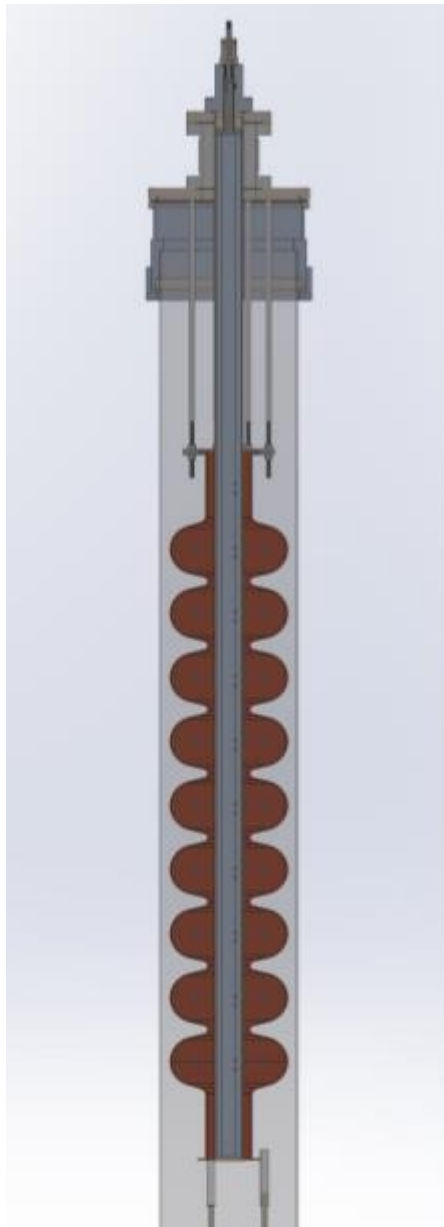


Figure 6.15 - Rotating magnetron for 9-cell cavity. In the centre of the cavity is visible the Nb cathode with inside the water-cooled rotating magnet.

Figure 6.16 shows a rendering of the magnetic configuration. As anticipated before, it consists in a “spiral” made of cylindrical NdFeB magnets with 5 mm diameters and 8 mm high, fitted onto a Nylon 6 holed cathode holder. One side of the spiral is composed by north oriented magnets (red face), the other side by south oriented magnets (blue face).

The magnetic field closes between the north and the south pole. The region between two cylindrical magnets, where magnetic field is parallel to the cathode surface, is the zone where plasma is more intense. Logically the rotation of the magnet pack guarantees a good target erosion and coating uniformity. There are 10 plasma horizontal regions (9 for the 9 cells of the cavity plus one for closing the magnetic confinements) visible on the central and right view of Figure 5.16. The

regions are connected between them in order to guarantee continuity of plasma, by vertical plasma region (left and right views) and used also for sputtering cavity cut off. The top and bottom horizontal plasma region are connecting between them to guarantee continuity of plasma region and not to lose electrons, through a vertical plasma region generated by the magnets visible on the rear parts of the magnet pack (right view onto Figure 6.16).

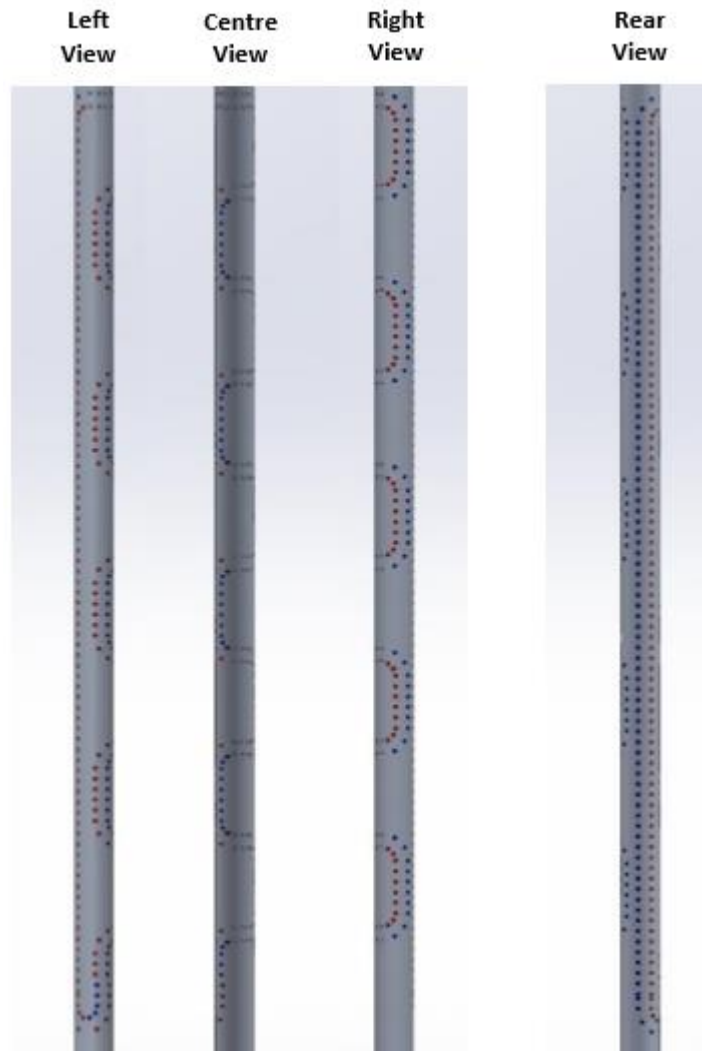


Figure 6.16 - Rendering of Nylon magnets holder rotated. In red the north pole of magnet, in blue south pole.

The described “spiral” configuration permits to have a constant deposition rate along the whole cavity. There is in fact a higher cathode erosion rate in the cavity cell regions (horizontal region confinements) that corresponds to a high cavity/cathode surface ratio to be coated and low cathode erosion rate along cavity cut-off (vertical region confinements).

Machining and assembly of the magnet pack was complex due to the need of drilling more than 500 holes and assembly 500 NdFeB magnets that compose it (Figure 6.17).

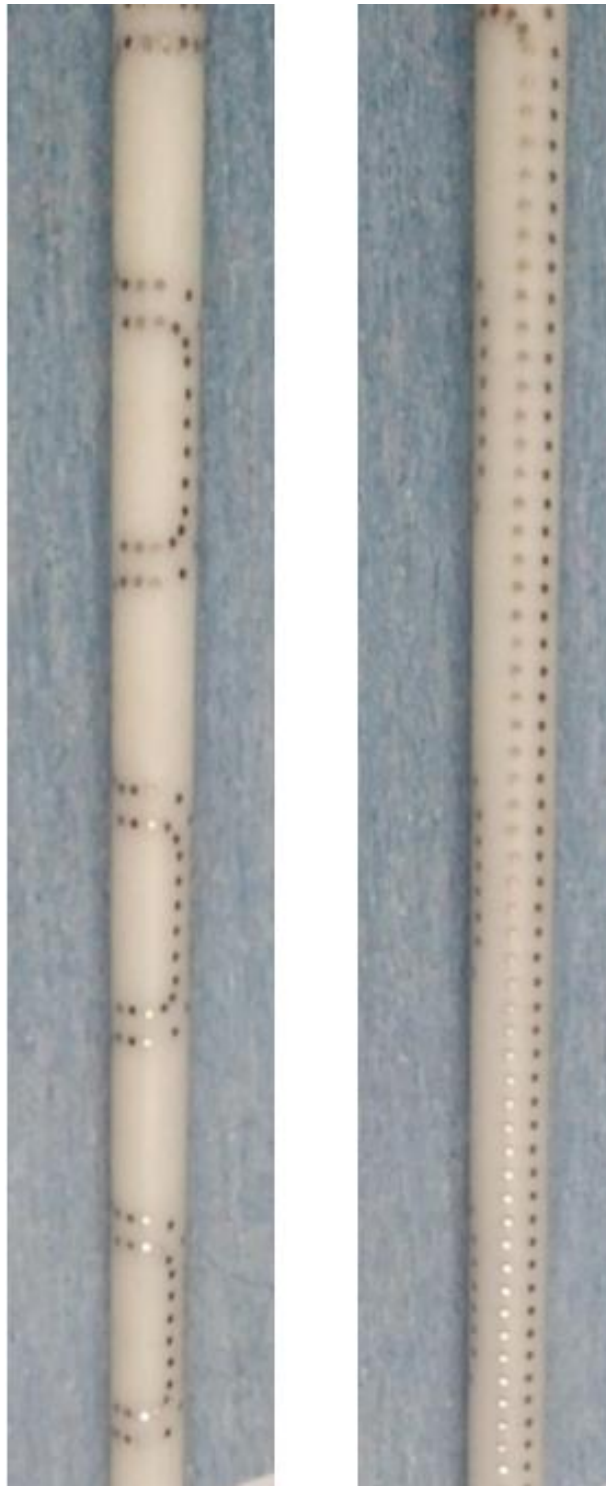


Figure 6.17 - Nylon 6 magnet pack assembled. On left front view, on right rear view.

6.7. Test with final internal magnetron, assembled in the system

After machining and assembling the internal magnetron was inserted to the system. For holding tests Stainless Steel cathode was used. This choice allows reducing costs respect to using Niobium

and it permits to evaluate the plasma confinements and the deposition rate of the source. In Figure 6.18 is visible the source completely assembled and ready for insertion inside vacuum chamber.

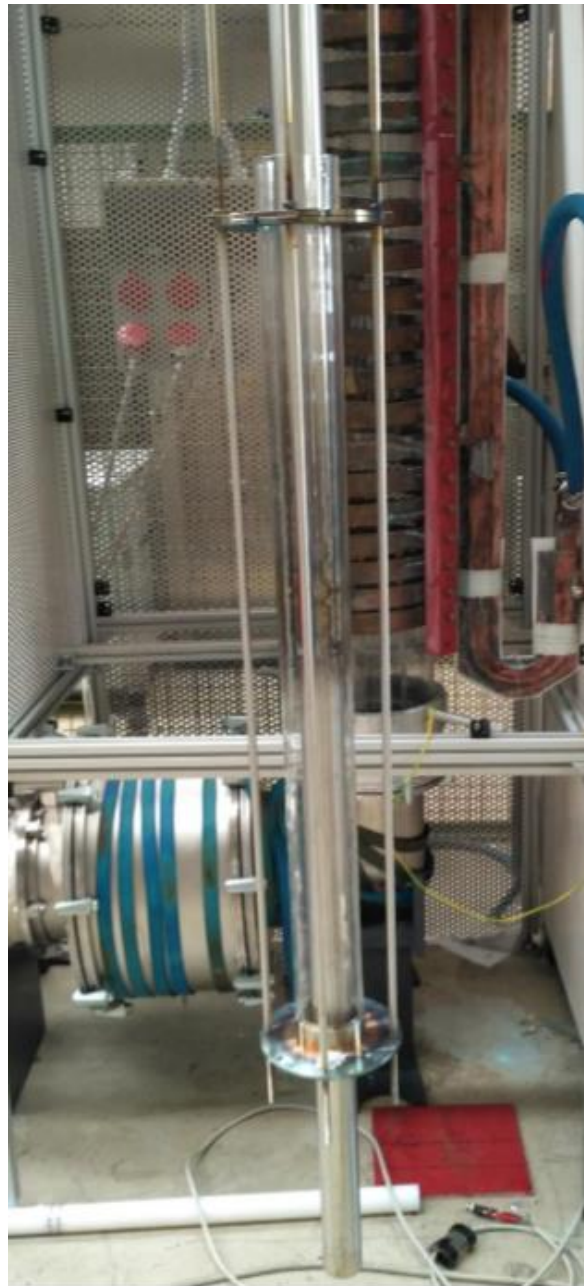


Figure 6.18 - Cathode assembled and ready for insertion inside the quartz vacuum chamber.

The four SS roods are used to support a quartz tube in order to protect the quartz chamber tube from deposition and, at the same time, to observe the plasma along the cathode.

In this test, the inductor is switched off because the magnetic field is generated by the permanent magnets and the induction will be used only for heating the cavity. The plasma is uniform along the 1.2 meter of the cathode and it makes a close path (Figure 6.19), fundamental aspect in order to produce a dense and confine plasma without electrons losses [8]. In the table 6.3 are being shown parameters of the test with final magnetron configuration.

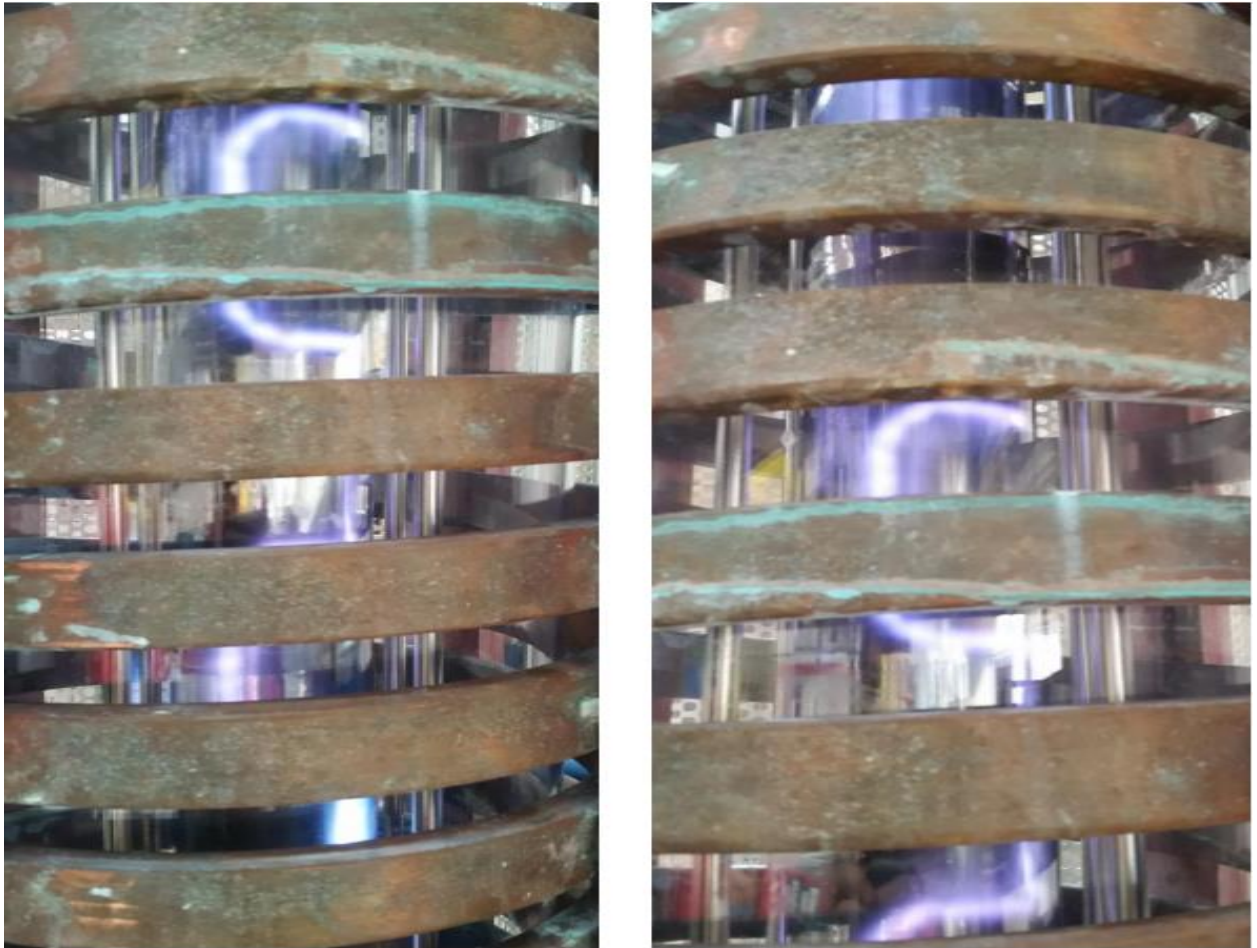


Figure 6.19 - Two different views of the plasma inside the vacuum chamber during preliminary test.

Table 6.3 – Sputtering parameters during test of the new magnetron construction

Parameter	Value
Sputtering tension	540 V
Sputtering current	1,6 A
Sputtering power	864 W
Inductor tension	-
Inductor current	-
Inductor power	-
Inductor frequency	-
Sputtering Ar pressure	$5 \cdot 10^{-2}$ mbar

6.8. Deposition rate measurements

Several test with different sputtering power and sputtering Ar pressure was made in order to evaluate deposition rate of the system. During this tests stainless steel was deposited onto the cleaned quartz pieces 10 x10 mm, that was placed opposite to the cathode. In the table 6.4 are being shown parameters of the tests of deposition rate measurements.

Table 6.4 – Sputtering parameters during tests of deposition rate measurements

Parameters		Test 1	Test 2	Test 3	Test 4	Test 5	Test 6	Test 7	Test 8
Sputtering tension	V	540	726	818	818	545	630	430	631
Sputtering power	W	1,6	10,9	2,9	3,98	15,04	13,5	19,1	23
Sputtering current	A	864	8000	2400	3500	8196	8196	8196	13500
Inductor tension	C	-	-	-	-	-	-	-	-
Inductor current	A	-	-	-	-	-	-	-	-
Inductor frequency	Hz	-	-	-	-	-	-	-	-
Inductor power	W	-	-	-	-	-	-	-	-
Sputtering Ar pressure	mbar	$5 \cdot 10^{-2}$	$1 \cdot 10^{-1}$	$7 \cdot 10^{-3}$	$1 \cdot 10^{-2}$	$4 \cdot 10^{-2}$	$3 \cdot 10^{-2}$	$5,5 \cdot 10^{-2}$	$4 \cdot 10^{-2}$
Time	min				60	20	30	30	30

After test the deposition rate of the deposited stainless steel coating was measured by the profiler DEKTAK 8. Results of the measurements had been shown on the Figure 6.20.

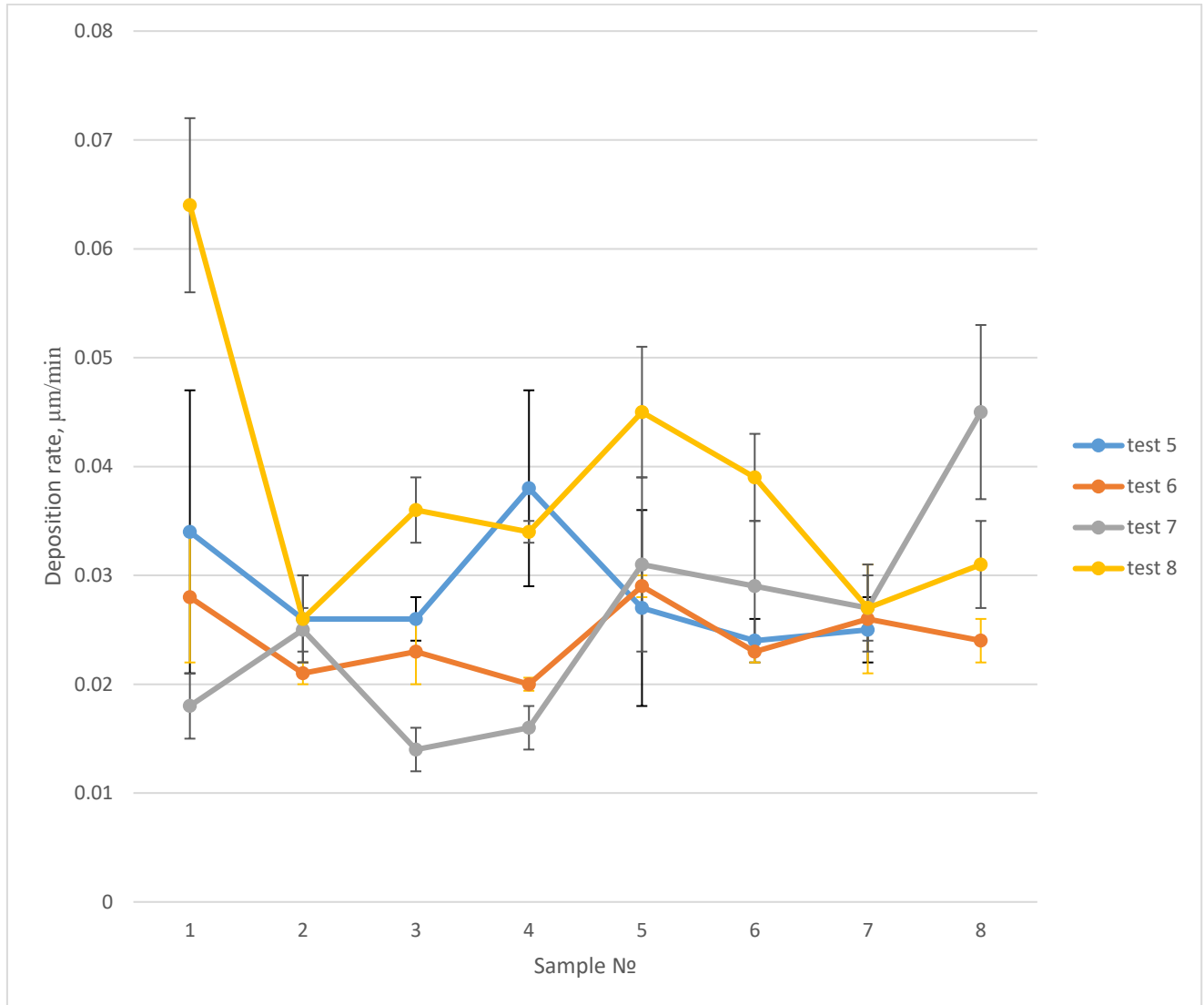


Figure 6.20 – Deposition rate of the system, that was measured at different sputtering parameters.

As it is shown on the Figure 6.20, deposition rate not very strongly dependant of the Argon pressure of the process. Curves of the tests 5,6,7, that were made at the different Ar pressures and at the same sputtering power, are very near to each other. On the other hand, power of the sputtering process is influence directly onto the deposition rate of the system. On the 6 of 8 samples higher deposition rate was obtained during test 8 ($P = 13\,500\text{ W}$), than during tests 5,6,7 ($P = 8\,196\text{ W}$).

6.9. Conclusion to the chapter

After the long work new system for niobium sputtering onto TESLA-type 9-cell RF cavities was made. In this system two magnetron assemblies have been used: external copper coil and internal magnetron with rotated system of magnets, inserted into the PVC tube. After assembling of the system, tests with quartz and copper shields were made. Also outgassing of the system were evaluated.

In this master thesis has been described only start of the work with this sputtering system. There are several possibilities to continue work in future. First of all, researching work in the field of optimisation of the construction of the magnetron will be held. Secondly, sputtering process with niobium target will be held. After that definition of the optimal parameters (Ar pressure during coating, power, magnet pack rotation frequency etc.) of niobium sputtering will be hold in order to obtain uniform thin film with good superconductive properties onto TESLA type 9-cell elliptical cavity [7].

CONCLUSION

Different configurations of cylindrical magnetrons were observed and investigated. There are different configurations of the cylindrical magnetron, but mostly they have one common aim: prevention of the material losses and intensification of the sputtering process by production of the magnetic field inside the vacuum chamber. Magnetron using in the sputtering system markedly increase deposition rate and greatly decrease working time of the sputtering process.

During researching work of Niobium sputtering onto 6 GHz cavities were obtained best results were obtained after holding the experiment № 3 at the third measurements in cryostat. In this case dependence $Q = f(E_{acc})$ is the most similar to the line from all made measurements and Q in this case is the highest. The worst result, that was obtained after holding cryostat measurements was in the experiment #1. In this case Q factor was the lowest and $Q = f(E_{acc})$ was presented as sharp slope. It can be explained by the bad quality of deposited Nb coating or not optimal sputtering parameters of the experiment.

During researching work of Niobium sputtering onto Quarter Wave Resonator successful attempt of sputtering was made. The system of niobium sputtering onto the quarter wave resonators was prepared, checked and tested.

During researching work of Niobium deposition onto TESLA – type 9-cell cavities several sputtering processes were successfully made. Several configurations of the internal magnetron were made and tested. Also outgassing of the system was evaluated. Deposition rate of the system at the different sputtering parameters (pressure and power) was defined.

Research and development, that were made in the work onto the system for Niobium deposition onto 6 GHz cavities is basic for the future work. During this work, optimal parameters of sputtering were defined. These parameters will be used in future work with the system of niobium sputtering onto TESLA-type 9-cell RF cavities. The idea of the rotated magnetron in the system of niobium sputtering onto TESLA-type 9-cell RF cavities was borrowed from the researching work of the system of niobium sputtering on the quarter wave resonators. The basic and the most complex researching work was done onto the system for niobium sputtering onto TESLA-type 9-cell RF cavities.

In this study was described only starting steps of the researching work in the field of High Vacuum technologies. For further work more time and strength will be needed, but there are a lot of very perspective possible researching lines in every of investigated systems, that can be taken as the basis in future scientific work.

Chapter 7

References

1. Evans L. Particle accelerators at CERN: From the early days to the LHC and beyond / Lyn Evans. // Technological Forecasting and Social Change. – Pages 4–12.
2. The International Linear Collider (2013, June 12). Retrieved from <https://www.linearcollider.org/>
3. Daniel Adrien Franco Lespinasse. (2015) AN INNOVATIVE CYLINDRICAL MAGNETRON SPUTTERING SOURCE FOR THE DEPOSITION OF Hf-ALN SUPERCONDUCTING Nb/Cu QWRs (Doctoral dissertation), The University of Ferrara.
4. Palmieri V. Superconducting resonant cavities / V. Palmieri. // European Training on Technologies and Industrial Applications of Superconductivity. – 1992. – Pages 224 – 255.
5. Padamsee H. RF Superconductivity for accelerators / H. Padamsee, J. Knobloch, T. Hays. – New York: Cornell University, Ithaca, 1998. – 523 p.
6. Stuart R. Vacuum Technology, Thin Films and Sputtering / R. V. Stuart. – Minneapolis, Minnesota: Koral Labs. Inc., 1983. – 151 p.
7. Hoffman, Dorothy M. Handbook of vacuum science and technology / Dorothy M. Hoffman, Bawa Singh, John H. Thomas, III. - 835 pages.
8. Giorgio Keppel. (2014/2016) Innovative PVD technologies for depositing superconducting Nb films into TESLA-type 9-cell RF cavities for particle accelerators (Doctoral dissertation), The University of Ferrara.